Results in Engineering 23 (2024) 102585

Contents lists available at ScienceDirect

Results in Engineering

journal homepage: www.sciencedirect.com/journal/results-in-engineering

Multiscale analysis of carbon nanotube-reinforced curved beams: A finite element approach coupled with multilayer perceptron neural network

Hossein Mottaghi T [a], Amir R. Masoodi [a,**], Amir H. Gandomi [b,c,*]

[a] Department of Civil Engineering, Ferdowsi University of Mashhad, Mashhad, Iran
[b] Faculty of Engineering & Information Technology, University of Technology Sydney, Sydney, Australia
[c] University Research and Innovation Center (EKIK), Óbuda University, 1034, Budapest, Hungary

ARTICLE INFO

Keywords:
Multiscale analysis
Free vibration
Carbon nanotubes (CNT)
Curved beams
Finite element method (FEM)
Multilayer perceptron (MLP)

ABSTRACT

This paper presents a comprehensive investigation into the structural response of curved composite beams enhanced with carbon nanotube (CNT). Employing a multiscale framework, our analysis leverages the finite element method (FEM) to account for both bending and shear deformations across six degrees of freedom. The inquiry encompasses diverse mechanical, geometrical, and boundary configurations to assess these composite beams' natural vibration features. Moreover, we introduce a multilayer perceptron (MLP) neural network architecture designed to forecast such beams' dimensionless first natural frequency. Trained on a meticulously curated dataset derived from FEM simulations, the neural network model exhibits promising predictive capabilities concerning the free vibration frequency. To ascertain the efficacy and precision of our proposed methodology, we conduct a comparative analysis between FEM results and employ statistical metrics to evaluate the neural network's predictive performance. The findings of this study reveal an impressive predictive accuracy of over 95 % with regards to the initial natural frequency of the composite beams, thereby emphasizing the potential effectiveness of neural network methodologies in engineering analyses. This study significantly contributes to advancing our comprehension of the vibrational dynamics inherent in carbon nanotube-reinforced composite beams, while concurrently underscoring the potential efficacy of neural networks in forecasting their dynamic attributes.

1. Introduction

Curved beams represent a blend of historical legacy and modern innovation in structural engineering, seamlessly combining aesthetics and efficiency. Their versatile applications across industries continue to intrigue researchers. Integrating carbon nanotubes into sandwich composite beams signifies a groundbreaking advancement, promising exceptional mechanical strength and design flexibility. This fusion of historical and contemporary elements signals a significant shift in structural engineering research, with investigations into the vibration behavior of curved beams offering transformative insights. Through this interdisciplinary approach, this research aims to pioneer innovative solutions in structural engineering applications.

The FEM revolutionized structural engineering by enabling accurate analysis of complex structures. Through discretization and mathematical equations, FEM optimizes designs and ensures structural safety, despite limitations. Here some articles related to the application of this method in the analysis of curved beams are discussed [1–5]. Rezaiee-Pajand and Rajabzadeh-Safaei developed a strain-based approach for curved beams, using a two-node beam element with six degrees of freedom. They demonstrated their effectiveness in accurately modeling parabolic members through numerical tests, which provided a precise understanding of their behavior [6]. Ghuku and Saha's review focused on the nonlinear behavior of curved beams under static loading, emphasizing the importance of numerical solutions in analyzing such behavior. They highlighted key parameters influencing the response and suggested directions for future research, particularly in microelectromechanical systems (MEMS) and nanoelectromechanical systems (NEMS) applications [7]. Upadhyay et al. investigated the behavior of curved beams under various loads, deriving force-displacement relationships for two-noded curved beam elements. Their work provided a practical framework for analyzing complex curved beam structures,

---

* Corresponding author. Faculty of Engineering & Information Technology, University of Technology Sydney, Sydney, Australia.
** Corresponding author.
E-mail addresses: hossein.mottaghi@mail.um.ac.ir (H. Mottaghi T), ar.masoodi@um.ac.ir (A.R. Masoodi), gandomi@uts.edu.au (A.H. Gandomi).

https://doi.org/10.1016/j.rineng.2024.102585
Received 3 June 2024; Received in revised form 7 July 2024; Accepted 17 July 2024

enhancing engineering practice in dealing with diverse loading conditions [8]. Choi and Lim introduced two curved beam elements that ensured freedom from locking characteristics, making them suitable for analyzing shallow and deep arches. Their simplicity, featuring only two nodes, enhanced usability in linear and geometrically nonlinear analyses [9]. Banan et al. formulated a FEM approach for spatial curved beams and arches on elastic foundations. Their method, which accommodated variable cross-sections and various load application methods, exhibited high accuracy and efficiency in structural analysis [10]. Savino and Tondolo proposed the inverse FEM for real-time structural monitoring with strain sensors, showing superior performance in numerical studies. This method holds promise for advancing structural health monitoring practices, pending further validation through experimental tests [11].

Also, Kim et al. presented a nodeless hybrid-mixed curved beam element, which outperformed conventional elements by eliminating stress oscillations and accurately predicting stress resultants. This element simplifies stiffness matrix equations and is particularly effective in numerical examples [12]. Yang et al. introduced the B-spline wavelet FEM for curved beams, offering insights into their static and free vibration characteristics. Their method, grounded in generalized shell theory, proved effective in analyzing curved beams with various curvatures and boundaries [13]. Tarn and Tseng's study examined stress and displacement fields in curved beams under in-plane loads, providing exact solutions for different end conditions. Their work emphasized the importance of precise analysis techniques, particularly for beams of strong orthotropic materials [14]. Kosmatka and Friedman developed a precise two-node FEM for curved shear deformable beams, effectively eliminating locking issues. This formulation showed improved accuracy and efficiency in both static and dynamic analyses, enhancing modeling accuracy across various beam geometries [15]. Tufekci, Eroglu, and Aya devised a FEM formulation addressing numerical errors and locking issues, demonstrating its superiority over existing methods in handling varying curvature and cross sections. Their approach also enables vibration analysis by integrating mass matrices into the formulation [16]. Sheikh introduced a horizontally curved beam element, incorporating shear strain to overcome locking issues. Validation through numerical examples showcased the element's accuracy and versatility, proving its stability and suitability for analyzing beams of various geometries [17]. Wang's development of the enhanced two-node curved beam element significantly improved mechanical analysis accuracy without additional computational burden. This element showed superior efficiency and accuracy over existing methods, particularly in significant curvature rate change cases, making it ideal for complex rod structures [18].

Free vibration in dynamic analysis entails the natural oscillatory motion of a structure without external forces. Understanding this phenomenon aids in assessing structural integrity and stability, which is crucial for engineering design. By analyzing natural frequencies and mode shapes, engineers optimize structures to withstand dynamic loads effectively [19–22]. Eisenberger and Efraim's research focused on determining the dynamic stiffness of uniform circular beams, which is crucial for accurately predicting their natural frequencies and dynamic behavior. By comparing their findings with established literature, they ensured the precision of their results, providing a reliable basis for further analysis and design considerations in structural engineering applications [23]. Rezaiee-Pajand and Rajabzadeh-Safaei's introduction of circular beam elements addressed the need for robust modeling tools to handle diverse beam scenarios, including infinite and thick beams. Their work demonstrated the accuracy and efficiency of these elements through comprehensive numerical testing, showcasing their reliability in capturing the complex behavior of curved structures under various loading conditions [24]. Wu and Chiang devised a practical method for obtaining stiffness and mass matrices for horizontally circular curved beam elements. Their approach, based on force-displacement and kinetic energy equations, simplified the assembly of global property matrices. Validation against existing solutions eliminated the need to replace curved elements with straight ones, simplifying structural analysis [25]. They also investigated natural frequencies and mode shapes of uniform circular arches using finite arch elements, showing high agreement with existing literature and close frequency alignment between straight and curved beam methods [26]. Yang et al.'s development of effective modeling methodologies for curved beams' in-plane vibration involved deriving governing differential equations and proposing practical solutions for numerical analysis. By accurately capturing the dynamic behavior of curved beams, their work provides valuable insights into the structural response under dynamic loading conditions, which is essential for assessing the structural integrity and performance of such systems [27]. Su et al.'s variational method for analyzing curved beams' vibration behavior significantly advances computational mechanics. By efficiently incorporating diverse boundary conditions and eccentric concentrated elements, their approach enables detailed analysis of complex structural systems, offering valuable insights into the dynamic response of curved beams under various loading scenarios [28]. Correa et al.'s exploration of the Generalized/Extended Finite Element Method (G/XFEM) for analyzing the free vibration of arched and curved beams demonstrates the method's potential for achieving accurate and efficient solutions, even with coarse meshes. Their findings provide valuable insights into the applicability of advanced numerical techniques for analyzing the dynamic behavior of curved structures in engineering practice [29]. Austin and Veletsos' simplified estimation method for in-plane vibration frequencies of circular arches offers a practical tool for structural engineers. By providing a straightforward approach to frequency estimation, their methodology facilitates the analysis and design of circular arch structures, particularly those exhibiting shear-flexible behavior [30]. Civalek and Kiracioglu's validation of the Discrete Singular Convolution (DSC) method for analyzing Timoshenko beam vibration problems highlights the method's effectiveness and potential for computational mechanics applications. Their work lays the groundwork for further advancements in numerical techniques for analyzing the dynamic behavior of complex structural systems [31,32]. Karamanli et al.'s investigation into the behaviors of 2D-FG curved beams sheds light on the influence of various factors, such as open angles and gradation indexes, on their structural characteristics. By understanding these influences, engineers can optimize the design and performance of curved beam structures, enhancing their structural efficiency and resilience [32].

In recent decades, the use of nanocomposites to enhance the performance of structural components has gained significant attention. Research conducted on these materials indicates that they significantly improve the performance of structural components by utilizing their two main constituents: the matrix material and the nanoscale filler. Sobhani et al. conducted a free vibration analysis of composite shells reinforced with carbon nanotubes (CNT) and graphene nanoplatelets (GNP) with a conical-cylindrical-conical sandwich cross-section using the first-order shear deformation theory. By employing Donnell's method and Hamilton's principle, they derived the governing equations and solved them using the Generalized Differential Quadrature Method (GDQM), examining the impact of geometric and material parameters on the natural frequency of the shells. Belarbi et al. studied buckling in functionally graded curved sandwich beams using a refined shear theory. Their Hermite-Lagrangian finite element model showed high accuracy, analyzing effects of boundary conditions, power-law index, curvature, and thickness ratios on buckling loads, setting a benchmark for future FG beam research [33]. Belarbi et al. proposed a refined shear deformation theory for functionally graded (FG) sandwich curved beams, utilizing a parabolic shear stress distribution without shear correction factors. Their finite element analysis covered three FG beam configurations, showing high accuracy and stability across varying thicknesses and providing key insights for future research on FG curved sandwich beams [34]. Guerroudj et al. studied the free vibration of functionally graded nanobeams using nonlocal higher-order shear deformation theory. They analyzed beams with varying material properties and derived governing equations for simply supported conditions. Their findings emphasized the significant influence of structural geometry, material gradients, and nonlocal parameters on vibration frequencies, crucial for future research [35].

Also, Frikha et al. expanded the Kirchhoff shell model to analyze non-linear bending in functionally graded carbon nanotube-reinforced composite shells (FG-CNTRCs) using three- and four-node finite elements. They investigated shells with uniform and graded CNT distributions (FG-V, FG-O, FG-X), determining material properties via a modified rule of mixtures. Numerical examples validated the model's predictive capability regarding CNT profiles, volume fractions, and geometric effects on non-linear behavior [36]. Zghal et al. studied the free vibration of functionally graded carbon nanotube-reinforced composite (FG-CNTRC) shells, examining various CNT distributions using a micro-mechanical model. They derived motion equations with a discrete double directors shell finite element approach and validated their model against different FG-CNTRC shell geometries. Their focus was on evaluating how CNT volume fractions and distribution profiles affect structural vibration characteristics [37]. Zghal et al. examined post-buckling behavior of functionally graded materials (FGM) and carbon nanotube-reinforced composites (FG-CNTRC). Using a double directors finite shell element model, they achieved high accuracy and low computational cost. Their study highlighted the effects of CNT reinforcements, load types, and geometrical parameters on post-buckling behavior, offering valuable insights for future research [38]. Kiarasi et al. investigated dynamic behavior of functionally graded CNTreinforced composite beams on viscoelastic foundations using higher-order shear deformation theory and Kelvin–Voigt viscoelastic model. They found significant stress reduction with viscoelastic foundation. Increasing foundation stiffness decreased beam displacement and increased vibration frequency, while higher damping effectively reduced vibration amplitude. Validation against prior research showed consistent results [39]. Zhao et al. investigated the natural frequencies of hybrid composite cylindrical shells reinforced with graphene platelets (GPLs) and carbon nanotubes (CNTs). Using a modified micromechanical model and finite element analysis, they assessed material properties and analyzed factors like layer count, reinforcement patterns, and geometric dimensions. Their findings highlight significant improvements in vibration behavior due to the combined use of CNTs and GPLs in these shells [40].

Machine learning applications in structural engineering offer predictive capabilities for behavior under various loads, optimize designs and enhance structural health monitoring. Challenges include data quality and algorithm interpretability, necessitating collaborative efforts for robust solutions. The integration of machine learning promises to advance structural engineering practices and improve efficiency and safety in infrastructure systems. Hajdú et al. used machine learning to predict elastic-critical lateral-torsional buckling moments in I-beams with sinusoidal corrugated webs. Models like CatBoost showed promising accuracy, surpassing traditional hand-calculation methods. This approach enhances the design process by efficiently determining crucial buckling parameters [41]. Sahib and Kovács optimized composite sandwich structures for high-speed train floors, focusing on weight and cost reduction. They used a multi-objective optimization model with a Genetic Algorithm and Artificial Neural Network. The model, validated with the Finite Element Method, achieved high accuracy. Results indicated significant weight savings using Carbon Fiber-Reinforced Plastic and Fiber-Metal Laminate face sheets, despite higher costs [42]. Aydin and Kisi investigated the potential of artificial neural network (ANN) in monitoring the structural health of beam-like structures. They utilized two types of ANN models, MLP and Radial Basis Neural Network (RBNN), to predict intact beam frequencies accurately and estimate crack parameters. This research aimed to provide a reliable method for nondestructive crack identification, which is crucial for maintaining structural integrity and safety [43]. Turan et al. delved into the behavior of functionally graded porous beams under diverse boundary conditions. They discovered that higher levels of porosity led to reduced natural frequencies and buckling loads in these beams. Employing analytical methods, FEM simulations, and ANN techniques, they aimed to comprehensively understand the mechanical response of such beams, essential for optimizing their design and performance in engineering applications [44]. Liu et al. proposed a novel approach for designing and optimizing curved beams using machine learning (ML) techniques. They aimed to achieve efficient designs across various optimization objectives by predicting nonlinear structure-property relationships. The experimental validation of their computational results through advanced 3D printing showcased the versatility and effectiveness of ML in structural optimization, indicating its potential to revolutionize design practices in civil engineering [45]. Fallah and Mohammadi Aghdam investigated the bending and free vibration behavior of three-dimensional functionally graded (TDFG) porous beams using physics-informed neural networks (PINN). Through Hamilton's principle and systematic hyperparameter tuning, they aimed to accurately model the complex effects of material distribution, porosity, and foundation on beam behavior. Their study provided valuable insights into optimizing the design and performance of TDFG porous beams for various engineering applications [46]. Mohanty et al. focused on understanding the dynamic behavior of circular and parabolic curved beams using Adaptive Neuro-Fuzzy Inference System (ANFIS) models. Their research aimed to estimate the natural frequencies of these beams through numerical simulations and empirical equations. By experimentally validating the ANFIS predictions, they demonstrated the accuracy and reliability of their proposed models, which could significantly enhance predictive capabilities in structural analysis and design [47]. Yu et al. developed a machine learning (ML) approach to optimize double-curved beam structures with bistable and negative stiffness features. By correlating thickness parameters with ML models, they aimed to improve mechanical properties and energy absorption capabilities. The findings of their research offer insights into enhancing the performance of metamaterial structures, with potential applications across various engineering disciplines [48]. Zhang and Xue investigated the design and mechanical property prediction of preflex beams using neural networks. Through FEM modeling and dataset creation, they aimed to accurately predict the mechanical characteristics of preflex beams. Their study emphasized the influence of design parameters such as arch height and thickness and showcased the benefits of incorporating a porous section to enhance specific absorbed energy, thereby expanding design possibilities for curved beams [49].

The literature review provides a detailed overview of past research on composite beams, with a specific focus on carbon nanotubes (CNTs) for mechanical reinforcement. Previous studies have contributed valuable insights into the static and dynamic properties of composite structures, but there are still gaps in our understanding of the multiscale behavior of curved beams that are reinforced with CNTs. Additionally, while FEM analysis has been extensively used to study the mechanical response of these beams, there is limited research on using neural network models to predict their dynamic characteristics. Therefore, this study aims to address these gaps by integrating FEM analysis and MLP neural networks. A novel and efficient approach has been introduced to predict the free vibration behavior of curved beams reinforced with carbon nanotubes, considering various mechanical and geometrical conditions. The neural network's performance has been evaluated using statistical indicators, and the obtained target value has been compared with the results obtained from the FEM. The results indicate the high accuracy of the modeled neural network in predicting the target value.

2. Effective mechanical properties on nanocomposites

In this study, a nanocomposite beam is reinforced with carbon nanotubes (CNTs) in which the agglomeration effect of these materials is taken into account. The beams is strengthened with CNT nanocomposites. Fig. 1 illustrates a general view of these types of beams. The influence of these materials on the nonlinear behavior of the beam and

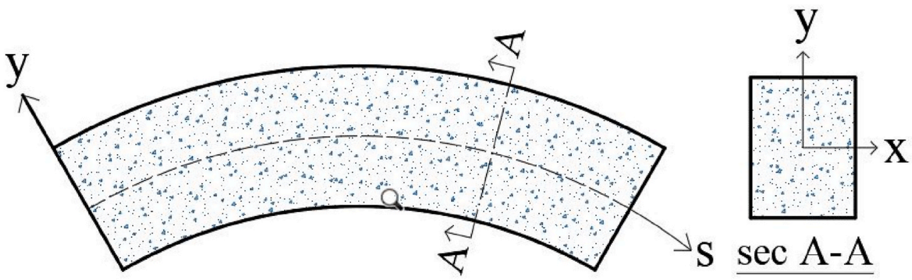

Fig. 1. Geometry of CNT curved beam.

their effective properties were estimated by Bui et al. using the Eshelby-Mori-Tanaka approach, where the effective elasticity and shear modulus are obtained for an equivalent homogeneous material [50]. Only the relationships used in this paper and the relevant parameters are mentioned here.

The assumption is that some of the CNTs are uniformly distributed (UD) throughout the matrix, while others appear clustered due to agglomeration. Fig. 2 illustrates the representative volume element (RVE) of it.

The total volume of CNTs can be divided into two parts:

$$V_r = V_r^{cluster} + V_r^m \tag{1}$$

where $V_r^{cluster}$ signifies the volume of CNTs contained within a cluster, and V_r^m signifies the volume of CNTs distributed in the matrix outside the clusters. The agglomeration is characterized by two parameters defined as follows:

$$\mu = \frac{V_{cluster}}{V} \tag{2-a}$$

$$\eta = \frac{V_r^{cluster}}{V_r} \tag{2-b}$$

In this context, V refers to the total volume of the representative volume element (RVE), and $V_{cluster}$ refers to the volume occupied by the cluster within the RVE. The symbol μ represents the proportion of the RVE's volume that is made up of clusters, while η indicates the proportion of the CNTs' volume that is located within the clusters relative to the entire volume of CNTs in the RVE. A value of $\mu = 1$ signifies that CNTs are evenly spread throughout the matrix, and a decrease in μ indicates increasing agglomeration of CNTs. When $\eta = 1$, all nanotubes are clustered together. If μ equals η, the volume fraction of CNTs within the clusters matches that outside the clusters, indicating complete dispersion. When η is greater than μ, a higher value of η denotes a more uneven spatial distribution of CNTs. The effective bulk and shear moduli of the clusters, as well as those of the matrix outside the clusters, are determined as follows:

$$K_{in} = K_m + \frac{V_{cnt}\eta(\delta_r - 3K_m\alpha_r)}{3(\mu - V_{cnt}\eta + V_{cnt}\eta\alpha_r)} \tag{3}$$

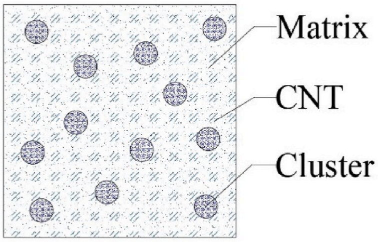

Fig. 2. RVE with Eshelby cluster model of agglomeration of CNTs.

$$K_{out} = K_m + \frac{V_{cnt}(1-\eta)(\delta_r - 3K_m\alpha_r)}{3[1 - \mu - V_{cnt}(1-\eta) + V_{cnt}(1-\eta)\alpha_r]} \tag{4}$$

$$G_{in} = G_m + \frac{V_{cnt}\eta(\eta_r - 2G_m\beta_r)}{3(\mu - V_{cnt}\eta + V_{cnt}\eta\beta_r)} \tag{5}$$

$$G_{out} = G_m + \frac{V_{cnt}(1-\eta)(\eta_r - 2G_m\beta_r)}{2[1 - \eta - V_{cnt}(1-\eta) + V_{cnt}(1-\eta)\beta_r]} \tag{6}$$

In these equations, The CNTs volume fraction V_{cnt} is assumed to vary in the beam thickness, and the remaining parameters are defined as follows:

$$\alpha_r = \frac{3(G_m + K_m) + k_r - l_r}{3(G_m + k_r)} \tag{7-a}$$

$$\beta_r = \frac{1}{5}\left[\frac{(4G_m + 2k_r + l_r)}{3(G_m + k_r)} + \frac{4G_m}{G_m + p_r} + \frac{2G_m(G_m + 3K_m) + 2G_m(7G_m + 3K_m)}{G_m(G_m + 3K_m) + m_r(7G_m + 3K_m)}\right] \tag{7-b}$$

$$\delta_r = \frac{1}{3}\left[n_r + 2l_r\frac{(2k_r + l_r)(2G_m + 3K_m - l_r)}{G_m + k_r}\right] \tag{7-c}$$

$$\eta_r = \frac{1}{5}\left[\frac{2}{3}(n_r - l_r) + \frac{8G_m p_r}{G_m + p_r} + \frac{8G_m m_r(4G_m + 3K_m)}{G_m(G_m + 7m_r) + 3K_m(G_m + m_r)} + \frac{2(2G_m + l_r)(k_r - l_r)}{3(G_m + k_r)}\right] \tag{7-d}$$

The subscripts m and r in the above equations represent the matrix and reinforcing phase, respectively. K_m and G_m are the bulk and shear modulus of the matrix, respectively. k_r, l_r, m_r, n_r, and p_r are Hill's elastic moduli for the reinforcing phase (CNT), listed in Table 1.

All geometric parameters associated with the beam and the related values used in ANN model can be found in Table 2. The effective bulk modulus K and effective shear modulus G of the composite material are calculated as follows using the Mori-Tanaka approach:

$$K = K_{out}\left(\frac{\mu\left(\frac{K_{in}}{K_{out}} - 1\right)}{\alpha(1-\mu)\left(\frac{K_{in}}{K_{out}} - 1\right) + 1} + 1\right) \tag{8}$$

$$G = G_{out}\left(\frac{\mu\left(\frac{G_{in}}{G_{out}} - 1\right)}{\beta(1-\mu)\left(\frac{G_{in}}{G_{out}} - 1\right) + 1} + 1\right) \tag{9}$$

where,

Table 1
Hill's elastic modulus for the CNTs [50].

Material	k_r (GPa)	l_r (GPa)	m_r (GPa)	n_r (GPa)	p_r (GPa)
CNT	30	10	1	450	1

Table 2
Geometric parameters of beams for the ANN model.

Parameter	Values
θ	π/4, π/2, 3π/4, π
R	1, 2, 3, 4, 5
R/h	2, 4, 6, 8, 10, 50

$$V_{out} = \frac{-2G_{out} + 3K_{out}}{2G_{out} + 6K_{out}} \tag{10-a}$$

$$a = \frac{V_{out} + 1}{3 - 3V_{out}} \tag{10-b}$$

$$\beta = \frac{8 - 10V_{out}}{15 - 15V_{out}} \tag{10-c}$$

Finally, the effective elasticity modulus E and effective Poisson's ratio ν are obtained as follows:

$$E = \frac{9GK}{G + 3K} \tag{11}$$

$$\nu = \frac{-2G + 3K}{2G + 6K} \tag{12}$$

It is worth mentioning that the presence of CNTs affects the mass density, and the following relationship holds:

$$\rho_{eff} = V_{cnt}\rho_{cnt} + V_m\rho_m \tag{13}$$

In this equation, the subscript m pertains to matrix properties. The mass density of the CNT phase ρ_{cnt} is considered to be 1780 kg/m^3 [51].

3. Developing finite element formulation

This paper considers a three-node circular curved element with a rectangular cross-section, along with two translational degrees of freedom and one rotational degree of freedom for each node. The geometric characteristics of the part are depicted in Fig. 3.

Each node has three displacements and three corresponding forces. The tangential displacement, radial displacement, and rotation of the cross-section about the normal axis of the beam plane are represented by u, v, and w, respectively. The axial strain ε, the shear strain γ, and the curvature κ are defined within the material model. The relationship between displacements and strains is as follows [52]:

$$\begin{Bmatrix} \varepsilon \\ \gamma \\ \kappa \end{Bmatrix} = \begin{bmatrix} \frac{\partial}{\partial s} & \frac{1}{R} & 0 \\ \frac{1}{R} & -\frac{\partial}{\partial s} & 1 \\ 0 & 0 & \frac{\partial}{\partial s} \end{bmatrix} \begin{Bmatrix} u \\ v \\ w \end{Bmatrix} \tag{14}$$

Based on Hooke's law for homogeneous and isotropic materials in the linear elastic range By utilizing the material matrix (D_M), stresses such as tangential stress σ_θ, shear stress τ, and radial stress σ_r can be obtained using the part's material properties.

$$[D_M] = \begin{bmatrix} AE & 0 & 0 \\ 0 & AkG & 0 \\ 0 & 0 & EI \end{bmatrix} \tag{15}$$

$$\begin{Bmatrix} \sigma_\theta \\ \tau \\ \sigma_R \end{Bmatrix} = [D_M] \begin{Bmatrix} \varepsilon \\ \gamma \\ \kappa \end{Bmatrix} \tag{16}$$

within the material matrix shown, the elastic modulus E, the shear modulus G, the area of the element's cross-section A, the moment of inertia about the neutral axis I, and the shear correction factor for this element k are represented. After obtaining stress values, by integrating over the part's cross-section, each of the axial force N, shear force V, and bending moment M becomes accessible [53].

$$N = \int_A \sigma_\theta dA = \int_{-\frac{h}{2}}^{\frac{h}{2}} E.\left(\frac{\partial u}{\partial s} + \frac{v}{R}\right).b.dy \tag{17}$$

$$V = \int_A \tau dA = \int_{-\frac{h}{2}}^{\frac{h}{2}} Gk.\left(\frac{u}{R} - \frac{\partial v}{\partial s} + w\right).b.dy \tag{18}$$

$$M = \int_A \sigma_R .y dA = \int_{-\frac{h}{2}}^{\frac{h}{2}} E.\left(\frac{\partial w}{\partial \theta}\right).y.b.dy \tag{19}$$

Now, the FEM formulation is discussed. Initially, a primary function is considered for each of the displacement fields. In this paper, the primary functions for each of these fields are assumed to be second-degree polynomials. It is observed that the First-Order Shear Deformation Theory (FOSDT) is employed to consider the shear deformation according to Timoshenko beam theory. Equation 20-a to 20-c represent these functions. In these equations, the parameter s denotes the arc length.

$$u_0 = a_1 + a_2 s + a_3 s^2 \tag{20-a}$$

$$v_0 = a_1 + a_2 s + a_3 s^2 \tag{20-b}$$

$$w_0 = a_1 + a_2 s + a_3 s^2 \tag{20-c}$$

where the vector of the nodal unknowns is assumed as follows:

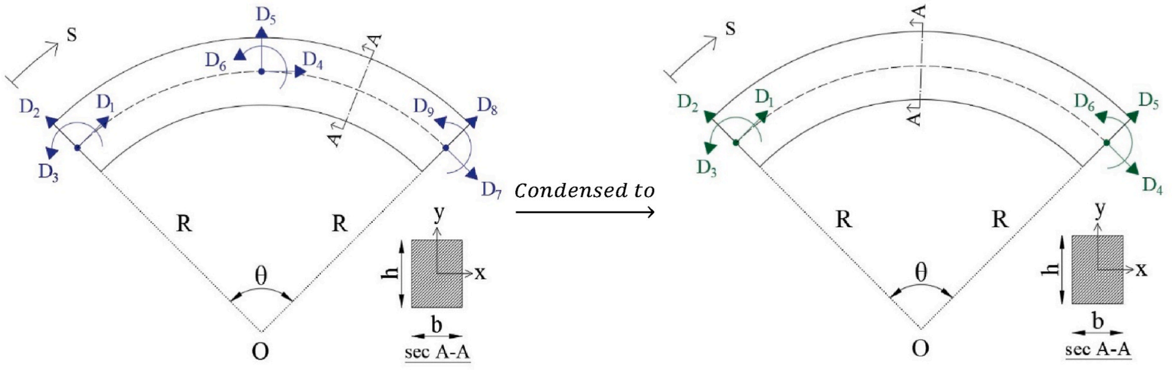

Fig. 3. The general form of a curved element before and after condensation.

$$q = \begin{bmatrix} a_1 & a_2 & a_3 \end{bmatrix}^T \tag{21}$$

To use the FEM formulation, the N_q matrix is accessible as follows:

$$[N_q] = \begin{bmatrix} 1 & 0 & 0 & s & 0 & 0 & s^2 & 0 & 0 \\ 0 & 1 & 0 & 0 & s & 0 & 0 & s^2 & 0 \\ 0 & 0 & 1 & 0 & 0 & s & 0 & 0 & s^2 \end{bmatrix} \tag{22}$$

Then, by substituting the value of s for each node in the primary displacement functions and replacing the arc length in terms of the central angle θ and radius ($L=R\theta$), the G_q matrix becomes accessible as follows.

$$[G_q] = \begin{bmatrix} 1 & 0 & 0 & 0 & 0 & 0 & 0 & 0 & 0 \\ 0 & 1 & 0 & 0 & 0 & 0 & 0 & 0 & 0 \\ 0 & 0 & 1 & 0 & 0 & 0 & 0 & 0 & 0 \\ 1 & 0 & 0 & 0.5R\theta & 0 & 0 & 0.25R^2\theta^2 & 0 & 0 \\ 0 & 1 & 0 & 0 & 0.5R\theta & 0 & 0 & 0.25R^2\theta^2 & 0 \\ 0 & 0 & 1 & 0 & 0 & 0.5R\theta & 0 & 0 & 0.25R^2\theta^2 \\ 1 & 0 & 0 & R\theta & 0 & 0 & R^2\theta^2 & 0 & 0 \\ 0 & 1 & 0 & 0 & R\theta & 0 & 0 & R^2\theta^2 & 0 \\ 0 & 0 & 1 & 0 & 0 & R\theta & 0 & 0 & R^2\theta^2 \end{bmatrix} \tag{23}$$

Now, the shape function matrix is obtained as follows:

$$[N] = [N_q].[G_q]^{-1} \tag{24}$$

$$[N] = \begin{bmatrix} N_1 & 0 & 0 & N_2 & 0 & 0 & N_3 & 0 & 0 \\ 0 & N_1 & 0 & 0 & N_2 & 0 & 0 & N_3 & 0 \\ 0 & 0 & N_1 & 0 & 0 & N_2 & 0 & 0 & N_3 \end{bmatrix} \tag{25}$$

$$N_1 = 1 - \frac{3s}{R\theta} + \frac{2s^2}{R^2\theta^2}, N_2 = \frac{4s}{R\theta} - \frac{4s^2}{R^2\theta^2}, N_3 = -\frac{s}{R\theta} + \frac{2s^2}{R^2\theta^2}$$

Finally, to obtain the stiffness matrix, interpolation functions for part strains are also required. According to the FEM formulation, using the differential operator matrix governing circular curved parts and integrating over the arc length, the B matrix the below shape:

$$[B] = \begin{bmatrix} \frac{\partial}{\partial s} & \frac{1}{R} & 0 \\ \frac{1}{R} & -\frac{\partial}{\partial s} & 1 \\ 0 & 0 & \frac{\partial}{\partial s} \end{bmatrix}.[N] \tag{26}$$

$$[B] = \begin{bmatrix} B_1 & B_2 & 0 & B_3 & B_4 & 0 & B_5 & B_6 & 0 \\ B_2 & -B_1 & RB_2 & B_4 & -B_3 & RB_4 & B_6 & -B_5 & RB_6 \\ 0 & 0 & B_1 & 0 & 0 & B_3 & 0 & 0 & B_5 \end{bmatrix} \tag{27}$$

$$B_1 = \frac{-3R\theta + 4s}{R^2\theta^2}, B_2 = \frac{1}{R} - \frac{3s}{R^2\theta} + \frac{2s^2}{R^3\theta^2}, B_3 = \frac{4(R\theta - 2s)}{R^2\theta^2}$$

$$B_4 = \frac{4s(R\theta - s)}{R^3\theta^2}, B_5 = \frac{-R\theta + 4s}{R^2\theta^2}, B_6 = \frac{s(-R\theta + 2s)}{R^3\theta^2}$$

Obtaining the part stiffness matrix can be done in two ways. The simpler method is the direct utilization of the FEM formulation. Equation (28) represents this process.

$$[K] = \int_s [B]^T.[D_M].[B]ds \tag{28}$$

Another method involves using the total potential energy function of the structure. Initially, the strain transformation functions with respect to the assumed degrees of freedom for the element are rewritten using Equation (30).

$$[D] = \begin{bmatrix} D_1 & D_2 & D_3 & D_4 & D_5 & D_6 & D_7 & D_8 & D_9 \end{bmatrix}^T \tag{29}$$

$$\begin{Bmatrix} u \\ v \\ w \end{Bmatrix} = [N].[D] \tag{30}$$

By substituting the matrices N and D into Equation (30), the displacement fields are obtained as follows:

$$u = D_1 \cdot \left(1 - \frac{3s}{R\theta} + \frac{2s^2}{R^2\theta^2}\right) + D_4 \cdot \left(\frac{4s}{R\theta} - \frac{4s^2}{R^2\theta^2}\right) + D_7\left(-\frac{s}{R\theta} + \frac{2s^2}{R^2\theta^2}\right) \tag{31}$$

$$v = D_2 \cdot \left(1 - \frac{3s}{R\theta} + \frac{2s^2}{R^2\theta^2}\right) + D_5 \cdot \left(\frac{4s}{R\theta} - \frac{4s^2}{R^2\theta^2}\right) + D_8\left(-\frac{s}{R\theta} + \frac{2s^2}{R^2\theta^2}\right) \tag{32}$$

$$w = D_3 \cdot \left(1 - \frac{3s}{R\theta} + \frac{2s^2}{R^2\theta^2}\right) + D_6 \cdot \left(\frac{4s}{R\theta} - \frac{4s^2}{R^2\theta^2}\right) + D_9\left(-\frac{s}{R\theta} + \frac{2s^2}{R^2\theta^2}\right) \tag{33}$$

After obtaining the strains, stresses, and moments using the differential operator matrix and integrating over the arc length, the total potential energy function of the structural deformation in terms of displacements becomes accessible.

$$U = \int_s \frac{EA}{2}\varepsilon^2 ds + \int_s \frac{kGA}{2}\gamma^2 ds + \int_s \frac{EI}{2}\kappa^2 ds - \sum_{i=1,9} P_i.D_i \tag{34}$$

Next, the part stiffness matrix is established, by employing the first theorem of Castigliano. According to the first theorem of Castigliano, the relative derivative of the total potential energy function of the structural deformation with respect to each displacement equals the corresponding dependent force. Essentially, the equations derived from this theorem represent the stiffness matrix. Equation (35) presents the mathematical representation of the first theorem of Castigliano. In this equation, P_i denotes the force corresponding to each degree of freedom.

$$\frac{\partial U}{\partial D_i} = P_i \tag{35}$$

In this paper, for brevity in the solution process, the direct utilization method of the FEM formulation is employed. It is noteworthy that both mentioned methods lead to the same result. Finally, the stiffness matrix K_l is represented as a 9x9 matrix in the local coordinate system of the element. This matrix is presented in Appendix A.

In structural analysis, sometimes it is necessary to reduce the number of degrees of freedom. The process of reducing degrees of freedom can be done at both the member and the entire structure levels. This reduction involves eliminating some of the degrees of freedom and altering the stiffness equations of the member or structure, resulting in a reduction in unknown variables and simplification of the calculation process. The forces resulting from this reduction in degrees of freedom are used for the remaining loads (such as typical nodal forces), and the effects of the removed forces are also considered. This process is carried out while maintaining the original analytical conditions, such as equilibrium, compatibility, and boundary conditions. The importance of this method lies in the fact that even if the effects of the removed degrees of freedom are not explicitly evident in the calculations, their effects are not forgotten and will be visible after calculating the remaining changes. Thus, in the process of reducing degrees of freedom, the effects of the removed degrees are considered and combined with the remaining degrees of freedom in the calculations. Therefore, after obtaining the stiffness matrix, to simplify the computational processes, by condensing the stiffness matrix and removing the intermediate nodes, the number of element degrees of freedom is reduced from 9 to 6. Using mathematical equations, the stiffness matrix after reducing degrees of freedom will be as follows [54]:

$$[K]\{D\}=\{P\}\Rightarrow\begin{bmatrix}K_{rr} & K_{re}\\ K_{er} & K_{ee}\end{bmatrix}\begin{Bmatrix}D_r\\ D_e\end{Bmatrix}=\begin{Bmatrix}P_r\\ P_e\end{Bmatrix} \tag{36}$$

$$[K_{eff}]=[K_{rr}]-[K_{re}][K_{ee}]^{-1}[K_{re}]^{T} \tag{37}$$

In these equations, the subscript r represents the remaining degrees of freedom, and the subscript e represents the removed degrees of freedom. The K_{eff} matrix is the stiffness matrix obtained after reducing degrees of freedom. Thus, the three-node curved part stiffness matrix is transformed into a 6x6 matrix. This matrix is represented in Equation (38).

$$[K_{eff}]=\begin{bmatrix}K_{11}^{eff} & K_{12}^{eff} & K_{13}^{eff} & K_{14}^{eff} & K_{15}^{eff} & K_{16}^{eff}\\ & K_{22}^{eff} & K_{23}^{eff} & K_{24}^{eff} & K_{25}^{eff} & K_{26}^{eff}\\ & & K_{33}^{eff} & K_{34}^{eff} & K_{35}^{eff} & K_{36}^{eff}\\ & & & K_{44}^{eff} & K_{45}^{eff} & K_{46}^{eff}\\ & sym & & & K_{55}^{eff} & K_{56}^{eff}\\ & & & & & K_{66}^{eff}\end{bmatrix} \tag{38}$$

The elements of the effective stiffness matrix K_{eff} are shown in Appendix A. Finally, the calculation of the element mass matrix is addressed. The presented equation in the FEM components for obtaining the mass matrix is as follows:

$$[m]=\rho\begin{bmatrix}A & 0 & 0\\ 0 & A & 0\\ 0 & 0 & I_x\end{bmatrix} \tag{39}$$

$$[M]=\int_s [N]^T.[m].[N]ds \tag{40}$$

In this equation, the parameter ρ represents the mass density of the material, and I_x is the moment of inertia of the section about the X-axis, which is calculated as follows for curved elements:

$$I_x=\int_A \frac{y^2}{1-\frac{y}{R}}dA \tag{41}$$

The lumped mass matrix is utilized with the aim of simplicity and efficiency. The lumped mass matrix for an element with 6 degrees of freedom is represented as a diagonal matrix:

$$[M]=0.5\rho\begin{bmatrix}A & A & I_y & A & A & I_y\end{bmatrix} \tag{42}$$

Finally, by solving the standard eigenvalue problem associated with the linear equation system, the natural frequencies of the curved beam composed of the presented elements in this paper can be obtained as follows.

$$\left|M-\omega^2K_{eff}\right|=0 \tag{43}$$

Fig. 4 shows the flowchart of determining the free vibration modes of a curved beam using the FEM.

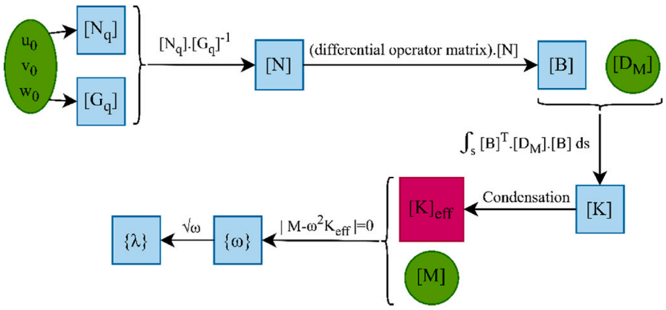

Fig. 4. Calculation steps of free vibration of bent beam using FEM.

4. Artificial neural network modeling

The ANN model is recognized as one of the most powerful computational techniques for predictive problems. Neural network-based algorithms present compelling advantages over traditional approaches such as tree-based algorithms and sparse kernel machine algorithms. Their innate ability to learn complex, nonlinear relationships within data, handle high-dimensional inputs, and generalize well to unseen data sets them apart. Additionally, ANNs offer scalability and parallelizability, making them suitable for large-scale datasets and real-time applications. By leveraging techniques like dropout regularization and parallel processing units, ANNs mitigate overfitting and enhance efficiency, leading to their widespread adoption across diverse domains. As research in ANN architectures and optimization techniques progresses, the dominance of ANNs in machine learning is expected to endure, driving further innovation and transformative advancements in artificial intelligence. The algorithm considered for this research is the MLP model [55]. MLP is a type of feedforward ANN composed of at least three neuron layers. Each neuron in a layer is connected to all neurons in the previous and next layers, calculates the weighted sum of its inputs, and then applies a nonlinear activation function. The input layer which is the first layer of the network, receives the data features as input. Each input node corresponds to a data feature or variable. The input layer performs no calculations; it simply transfers the inputs to the next layer. This layer determines the dimensions of the input data, which affects the number of parameters and the network's complexity. After leaving the input layer, the data proceeds to the hidden layers. The hidden layers are responsible for learning patterns and complex, nonlinear features from the data. These layers can be seen as a set of transformations that map the input space to the output space. Additionally, by applying a nonlinear activation function, intermediate computations, and transformations are performed on the data. Each neuron contains an activation function and a bias. The input vector of a neuron is denoted by j, and the weighted sum of inputs by Q, represented as:

$$Q=\sum_{i=1}^{d} w_i j_i = Wj+b \tag{44}$$

where W is the weight vector with dimension d, and b is the bias. Nonlinear processing must be applied to Q to represent the nonlinear relationship between input and output layers. This is accomplished by the activation function. The activation function is a crucial component of the network that introduces nonlinearity to the model and enables it to learn complex mappings between inputs and outputs. Each neuron in the hidden and output layers of the ANN uses an activation function to apply nonlinear mappings to the network. Fig. 5 illustrates the process taking place in each neuron.

There are several kinds of activation functions. The choice of activation function depends on the task, data, and network architecture, often requiring experimentation to determine the most suitable ones. In

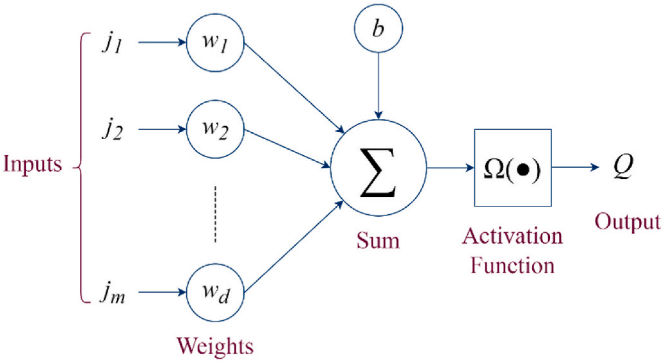

Fig. 5. Simplified scheme of an artificial neuron.

this network, the Selu activation function is used, defined as follows:

$$Selu(x) = \begin{cases} \lambda x & x \geq 0 \\ \lambda\alpha(e^x - 1) & x < 0 \end{cases} \tag{45}$$

where λ and α approximately have the following values.

$$\lambda = 1.0507009874$$

$$\alpha = 1.6732632424$$

Fig. 6 illustrates this function in Cartesian coordinates.

The output layer, the last layer in the ANN, is responsible for generating the model estimations. The design of the output layer depends on the nature of the task and the specific requirements of the problem under investigation. The output layer is connected to the last hidden layer with weights and biases, which are adjusted during the training process. Additionally, this layer calculates an error function; the model attempts to minimize the error by adjusting the weights and biases using a learning algorithm. The choice of error function depends on the type of output and the model's task. The goal of an ANN is to learn optimal weights and biases for connections between neurons, enabling the network to minimize the error between its outputs and the desired outputs for a set of inputs. This is achieved using a learning algorithm, such as backpropagation, which iteratively adjusts the parameters based on the gradient of a loss function. In this network, the Mean Squared Error (MSE) loss function is used, defined as:

$$MSE = \frac{1}{n}\sum_{i=1}^{n}(p_i - t_i)^2 \tag{46}$$

where n is the total number of data points, p_i and t_i represent the target value and the predicted value for the ith data point, respectively.

Now, the application of this type of ANN in this study is addressed. Considering the assumptions of the problem, some mechanical and geometrical properties related to the curved beam are provided as inputs to the ANN model, and the ANN's objective is to estimate the first dimensionless natural frequency. It is worth mentioning that to make the frequency dimensionless, the actual value of the natural frequency must be multiplied by a coefficient $l^2\sqrt{(\rho A/EI)}$. Since different support conditions are considered for the beam, including four traditional simple-simple (S–S), clamped-clamped (C–C), clamped-simple (C–S), and clamped-free (C–F) modes, it needs to be encoded first. The One-Hot encoding method is one of the most common approaches which its performance is excellent except when the categorical variable takes very large values. The One-Hot encoding creates new binary columns, each corresponding to one of the values the variable takes. This method is used to apply the support condition variable to the ANN model. Fig. 7 illustrates the encoding of support conditions for this network.

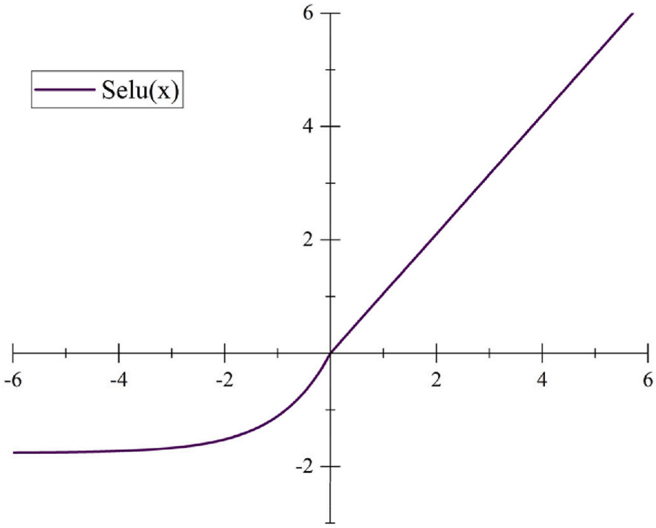

Fig. 6. Activation functions of the ANN model.

The assumed material for the matrix in this study is ordinary concrete with a mass density ρ_m=2777 kg/m^3. According to ACI-318-08 regulations, the value of the concrete's elastic modulus is obtained from the relationship $E_c=4700\sqrt{f'_c}$ in terms of MPa [56]. In this equation, f'_c represents the compressive strength of the concrete at 28 days using standard cylinders with a diameter of six inches and a height of twelve inches. Therefore, the young's modulus of the assumed material for the matrix is variable according to the value of f'_c. Considering a Poisson's ratio ν equal to 0.3 for concrete, the values of the shear modulus (G_m) and bulk modulus (K_m) for homogeneous linear elastic materials can be obtained for each modulus of elasticity and Poisson's ratio, respectively, using equations 47 and 48.

$$G_m = \frac{E}{2(1+\nu)} \tag{47}$$

$$K_m = \frac{E}{3(1-2\nu)} \tag{48}$$

In this article, the input to the ANN is the compressive strength of concrete. Therefore, the shear modulus and bulk modulus of the matrix, which are necessary for calculating the effective modulus of elasticity and effective shear modulus of the composite material, are made available as described. It should be noted that compressive strength values of 20, 30, 40, and 50 MPa are considered as inputs to the ANN. The volume fraction of clusters with respect to the total RVE (μ), the volume ratio of CNTs inside the clusters over the total CNTs within the RVE (η), and the volume fraction of CNTs inside the beam (V_{cnt}) are other inputs to the ANN. The values of 0, 0.1, 0.2, 0.3, 0.4, and 0.5 are considered for each of the μ and η parameters, and the values of 0, 0.12, 0.17, and 0.28 are considered for the V_{cnt} parameter. Three other inputs to the ANN are related to the geometrical properties of the curved beam. These variables are the central angle θ, the radius R, and the ratio of the radius to the beam height R/h, for which the values are specified in the table below.

It should be noted that the width of the rectangular cross-section of the curved beam is equal to 0.75 times the height of the cross-section, and the shear correction factor is assumed to be 5/6.

Therefore, each of these variables changes within a specified range, and a total of 276,480 data points are generated for the curved beam from 5 elements. After performing the calculations, using the equations obtained from the FEM, the final solution to the problem, which is the first dimensionless natural frequency of the curved beam, is obtained for various permutations of these properties and conditions. In this way, the data for the network, including input variables and target values, are made available. Additionally, to improve the model accuracy, the database is standardized. Data standardization helps to ensure that their importance is independent of their measurement unit. Even if the data have a normal distribution, standardizing them to standard scores can still be useful. The Z-score standardization is used to transform data from a normal distribution to a standard normal distribution. The relationship between the standard score and the actual value is as follows:

$$z_i = \frac{x_i - \frac{1}{n}\sum_{i=1}^{i=n}x_i}{\sigma} \tag{49}$$

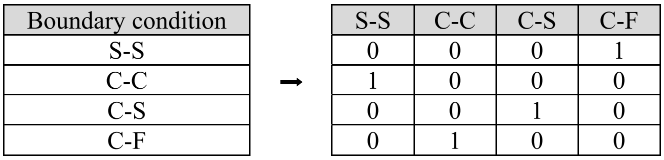

Boundary condition
S-S
C-C
C-S
C-F

➡

S-S	C-C	C-S	C-F
0	0	0	1
1	0	0	0
0	0	1	0
0	1	0	0

Fig. 7. One-hot encoding of beam support conditions.

In the above equation, z_i is the standard score for data x_i, and σ is the standard deviation of the data. By doing this, the z_i have a mean of 0 and a variance of 1. Then, by selecting 15 % of the data as test data, these values are specified as input data, and the first dimensionless natural frequency λ_1 of the curved beam for each of the input vectors is determined as the target value for the ANN. Fig. 8 shows the architecture of the proposed ANN model. In this model, eleven neurons in the input layer represent eleven input parameters mentioned earlier, and one neuron in the output layer represents the network's objective value.

It is worth noting that the number and size of hidden layers affect the performance and generalization ability of the ANN. There is no definitive rule for selecting the optimal architecture, but exploratory and empirical methods can be used. The ANN coding in this study was done using Python. The ANN model is created using the Keras library, and the most optimal network in terms of the number of layers and neurons is modeled using the Keras-Tuner module. Finally, by considering 15 % of the total data as validation data, the overfitting or underfitting of the network is controlled using validation data evaluation to ensure that it does not occur. By examining the responses of the validation data, the performance of the network is discussed. In this way, using the created ANN, it is possible to estimate the behavior of the curved beam under various geometrical, mechanical, and support conditions.

5. Performance of the ANN

Fig. 9 illustrates the performance of the developed ANN model, where the MSE decreases with increasing epochs for both training and validation data. The MSE value at epoch 400 is approximately 0.0209, which is very close to zero. Also, the convergence of the error function for these two datasets indicates that there is no overfitting or underfitting of the network, and the ANN model has been trained very well.

Fig. 10-a, 10-b, and 10-c compare the dimensionless first natural frequency of the curved beam obtained from the ANN model and the numerical data resulting from FEM analysis for training, testing, and whole of data. These charts show that the absolute values of errors are mostly less than 3 %, and the proposed model exhibits satisfactory accuracy in estimating the target values.

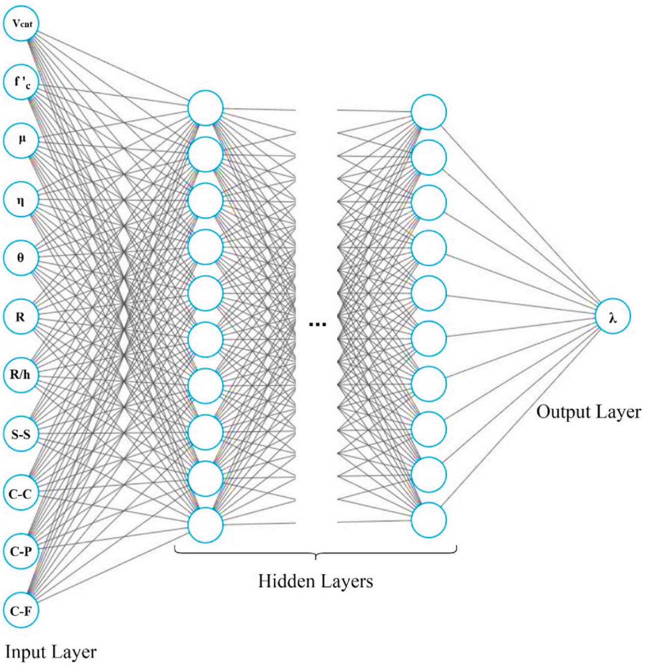

Fig. 8. Illustrative architecture of the ANN model.

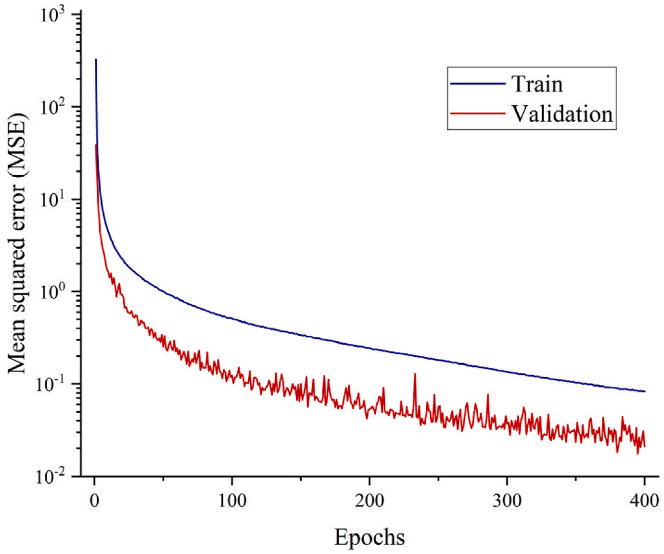

Fig. 9. Performance of the ANN model.

In this study, indices such as Root Mean Square Error (*RMSE*), Mean Absolute Percentage Error (*MAPE*), coefficient of determination (R^2), Relative Root Square Error (*RRSE*), Relative Absolute Error (*RAE*), and performance index (*PI*) have been used to evaluate the ANN model performance. These indices are calculated using the following equations.

$$RMSE = \sqrt{\frac{1}{n}\sum_{i=1}^{i=n}(t_i - o_i)^2} \tag{50}$$

$$MAPE = \frac{100}{n}\sum_{i=1}^{i=n}\left(\frac{t_i - o_i}{t_i}\right) \tag{51}$$

$$R^2 = 1 - \frac{\sum_{i=1}^{i=n}(t_i - o_i)^2}{\sum_{i=1}^{i=n}\left(t_i - \frac{\sum_{i=1}^{i=n}t_i}{n}\right)^2} \tag{52}$$

$$RRSE = \sqrt{\frac{\sum_{i=1}^{i=n}(t_i - o_i)^2}{\sum_{i=1}^{i=n}\left(t_i - \frac{\sum_{i=1}^{i=n}t_i}{n}\right)^2}} \tag{53}$$

$$RAE = \frac{\sum_{i=1}^{i=n}|t_i - o_i|}{\sum_{i=1}^{i=n}\left|t_i - \frac{\sum_{i=1}^{i=n}t_i}{n}\right|} \tag{54}$$

$$PI = \frac{RMSE \Big/ \frac{1}{n}\sum_{i=1}^{i=n}t_i}{1 + R} \tag{55}$$

In these equations, the target values are denoted by t_i and the output of the ANN by o_i. These indices have been calculated for training, testing, and all data, and the results are shown in Table 3.

The R^2 values for training, testing, and all data are 0.999944, 0.999942, and 0.999943, respectively. It can be observed that these values are close to 1, highlighting the proper performance of the proposed ANN model. In other words, the ANN model is highly reliable in estimating the first dimensionless natural frequency of the curved beam.

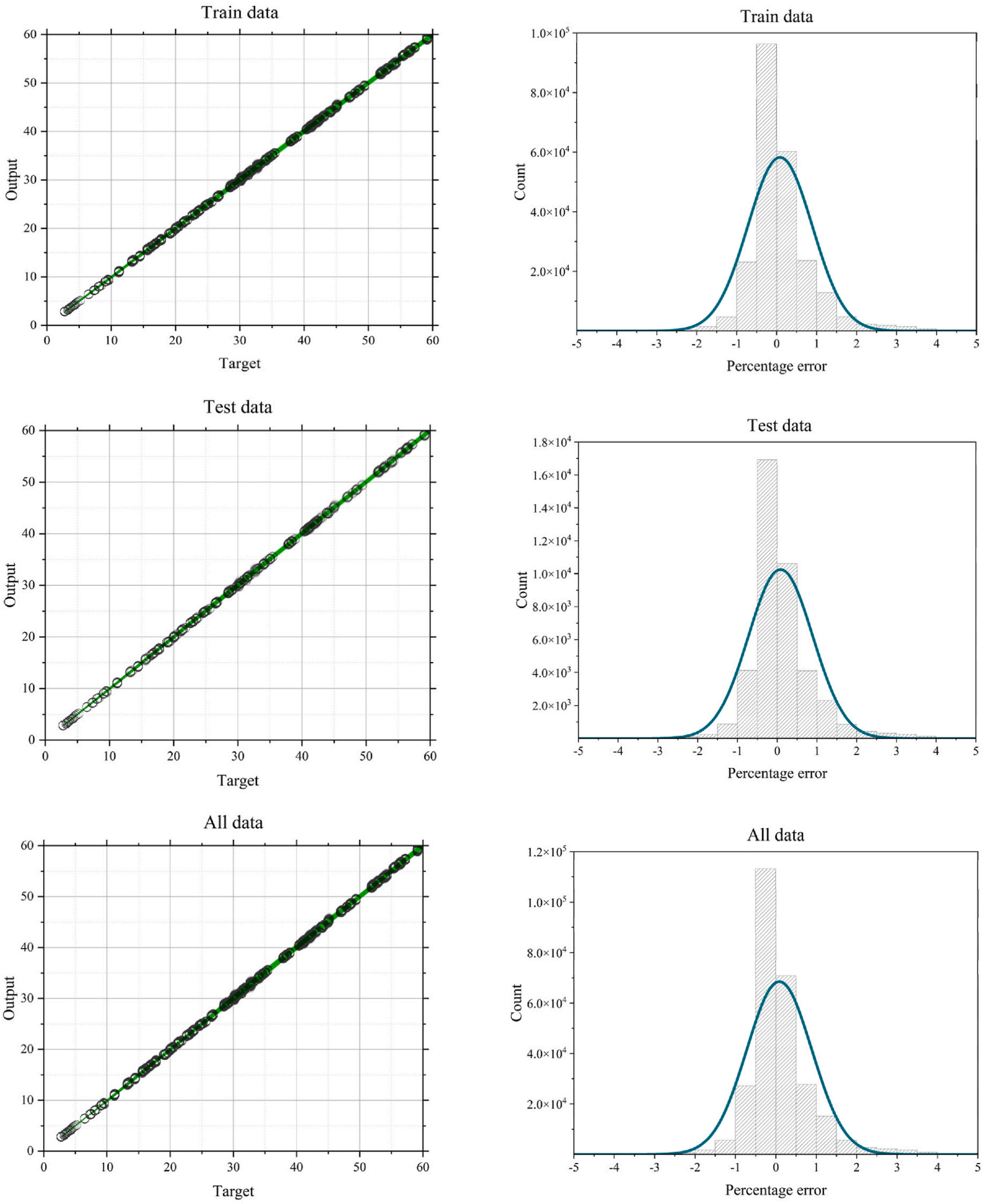

Fig. 10. a. Performance of train data. b. Performance of test data. c. Performance of all data.

Table 3
Statistical metrics indicating ANN performance.

Data	*RMSE*	*MAPE*	R^2	*RRSE*	*RAE*	*PI*
Train	0.203562	0.005617	0.999944	0.007515	0.006879	0.003350
Test	0.205377	0.005664	0.999942	0.007619	0.006960	0.003385
All	0.203835	0.005624	0.999943	0.007530	0.006891	0.003355

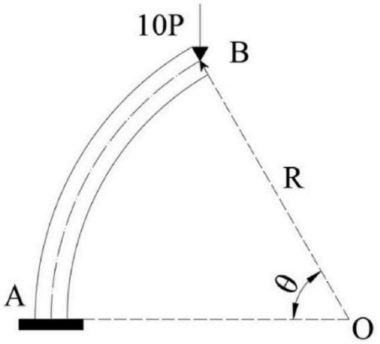

Fig. 11. The geometry of the circular arch.

6. Numerical studies

6.1. Static test

A single-supported circular arch with central angle θ and radius R, as shown in Fig. 11, is subjected to a vertical load of $10P$. The flexural stiffness of the structural section is EI. The solution to this example was performed by Rezaiee-Pajand et al. [57]. using the virtual work method, resulting in the following value for the rotation at point B in the clockwise direction.

$$\alpha_B = 10\frac{PR^2}{EI}(\sin[\theta] - \theta\cos[\theta]) \tag{56}$$

By substituting $\theta=\pi/3$, $p=10\ Ton$, $R=500$ cm, $E=2\times10^6\ kg/cm^2$, and $I=8360$ cm^4, the value of 0.512 radians is obtained for the rotation at point B. By substituting the mentioned values for the central angle of the arch, load, radius, modulus of elasticity, and moment of inertia in the FEM equations, the rotation of the desired node is investigated. Fig. 12 illustrates the convergence of this value to its exact value.

Table 4 shows the percentage error of the rotation at point B relative to its exact value for different numbers of beam elements. As observed, with 4 elements, the error percentage drops below 1 %. The results of this example demonstrate that the stiffness matrix is well-established and exhibits satisfactory convergence.

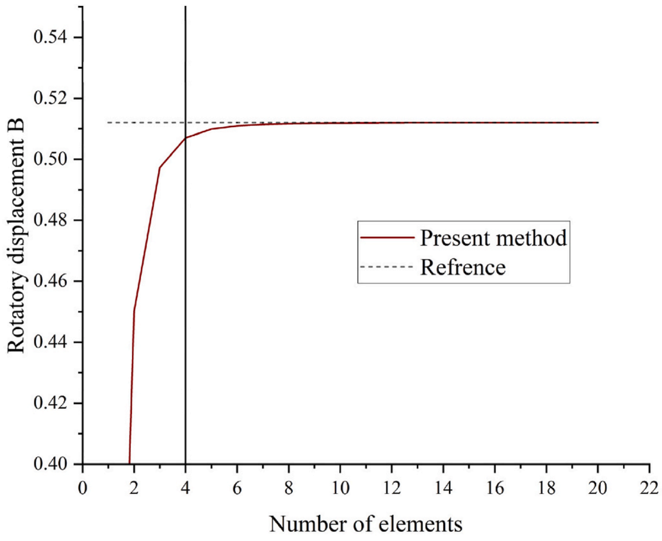

Fig. 12. Convergence of rotation response at point B.

Table 4
The error of rotation at point B for beams with different element counts.

Number of Elements	Rotatory displacement B (Rad)	Percentage error
1	0.1746	65.8965
2	0.4501	12.0804
3	0.4972	2.87655
4	0.5069	0.97841
5	0.5098	0.41629
6	0.5109	0.20536
7	0.5114	0.11247

Table 5
Geometric specifications of beams.

Boundary condition	R (m)	A (m^2)	I (m^4)
S–S	0.75	4	0.01
C–C	0.6366	1	0.0016

Table 6
The first five dimensionless natural frequencies of beams for S–S and C–C support conditions.

Boundary conditions	Mode number (i)	Present method (20 elements)	Ref [24]	Ref [27]	Ref [23]
S–S	1	29.2641	29.285	29.306	29.28
	2	33.2805	33.321	33.243	33.305
	3	66.9349	67.202	67.123	67.124
	4	79.8174	80.049	79.95	79.971
	5	107.1096	108.169	107.844	107.851
C–C	1	36.6742	36.716	36.657	36.703
	2	42.2276	42.278	42.289	42.264
	3	81.9305	82.361	82.228	82.233
	4	84.3283	84.565	84.471	84.491
	5	121.3303	122.722	122.298	122.306

6.2. Experiment on the first dimensionless natural frequency

This section analyzes two semi-circular beams, one with simple-simple support conditions and the other with clamped-clamped conditions. The mechanical properties $E=70$ GPa, $k=0.85$, $\upsilon=0.41666$, and $\rho=2777$ kg/m^3 are the same for both support conditions. The structural details and cross-section of each of these two beams are presented in Table 5.

To find the first dimensionless natural frequency, a beam with 20 elements is utilized. In Table 6, the author's results are compared with those obtained by Rezaiee-Pajand and Rajabzadeh Safaei (2016), Yang et al. (2008), and Eisenberger and Efraim (2001).

Figs. 13 and 14 illustrate the convergence of the first dimensionless natural frequency obtained from this study with the results obtained by Eisenberger and Efraim (2001).

As observed, the obtained responses demonstrate satisfactory convergence.

6.3. Presented ANN model experiment

In this section, two different beams are defined to evaluate the ANN model performance when their conditions do not match with any of the model data. For these two beams, $f'_c=25$ MPa and $R/h=3.2$, and other specifications are provided in Table 7.

Table 8 illustrates the responses obtained from the FEM, the ANN model output, and the percentage of error between them. Considering the low error value, it can be concluded that the ANN has been well-trained, and its estimation for natural frequency is reliable.

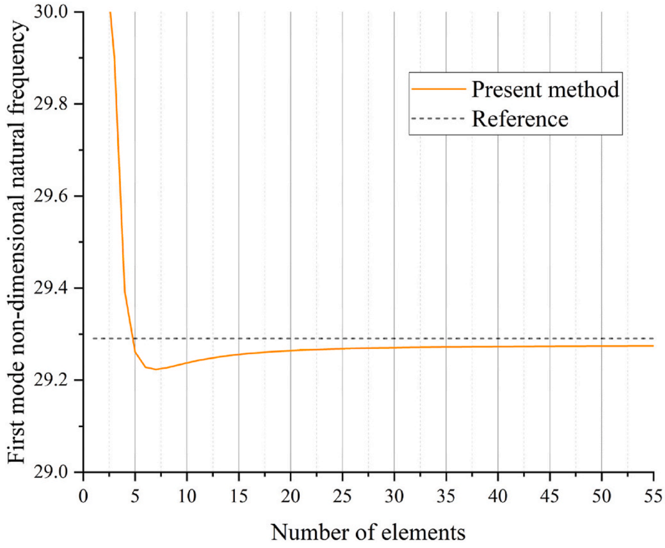

Fig. 13. Convergence of response for the first vibration mode under simple-simple support conditions.

7. Parametric studies

To investigate the impact of the radius-to-depth ratio of a beam on its natural frequency, a parametric study is conducted. For this purpose, the dimensionless first natural frequency chart of the beam for various values of the radius-to-depth ratio is plotted under different boundary conditions. This beam is semi-circular, and the mechanical properties of the homogeneous material are E = 70 GPa, k = 0.85, $\nu = 0.41666$, and $\rho = 2777$ kg/m^3. A constant radius of R = 10 m is considered for the beam. According to Fig. 15, it can be observed that as the radius-to-depth ratio increases, the beam becomes thinner, resulting in a decrease in stiffness. With the reduction in stiffness, the natural frequency of the beam also decreases. Also, based on the results, the natural frequency values for a beam with different boundary conditions are as follows:

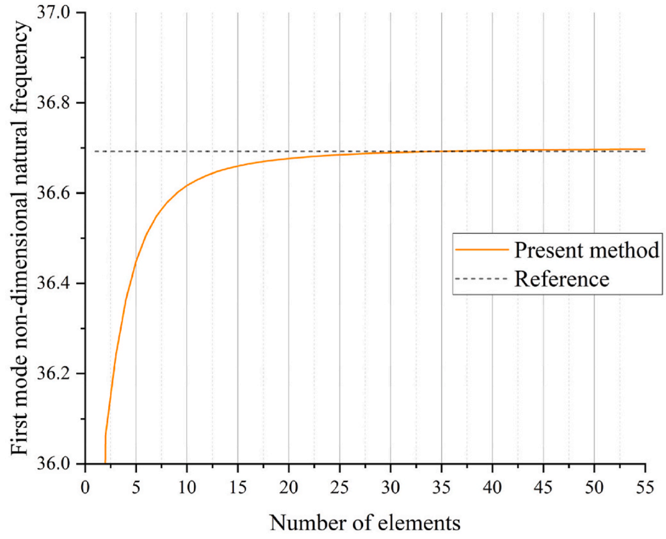

Fig. 14. Convergence of response for the first vibration mode under clamped-clamped support conditions.

Table 7
Specifications of curved beams.

Beam No.	Boundary condition	μ	η	V_{CNT}	θ	R
1	*P–P*	0.31	0.19	0.28	π/4	4.3
2	C–C	0.47	0.8	0.12	π	7

Table 8
The result of the FEM and ANN methods on the estimation of natural frequency.

Beam No.	Natural frequency obtained from FEM	Natural frequency obtained from ANN	Percentage error between FEM and ANN
1	24.9988	24.6717	1.3082
2	38.0412	38.1891	−0.3887

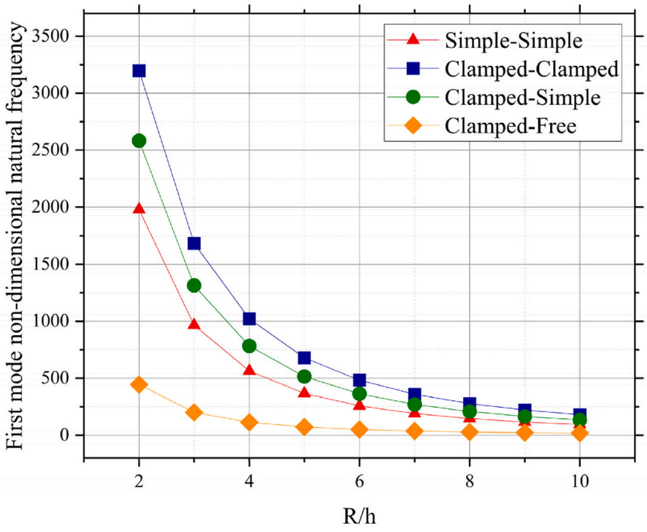

Fig. 15. The effect of the R/h ratio on the dimensionless first natural frequency of a curved beam under different boundary conditions.

$$C - C > C - S > S - S > C - F$$

A parametric study was conducted to evaluate the effects of the volume ratio of CNTs inside the clusters over the total CNTs within the RVE (η) on the first natural frequency of the beam for various values of the volume fraction of clusters with respect to the total RVE (μ). For this purpose, the variable considered varied from the minimum to the maximum range relevant to the ANN data, and for other variables of the problem, the values of $V_{cnt}=0.12$, f'_c=30 MPa, $\theta=\pi$, $R=3$ *m*, and $R/h=4$ were considered. Fig. 14 illustrates this effect for four different support conditions. According to Fig. 16, it is evident that the variation in the first mode of free vibration of the beam is more pronounced in the C–C and C–S support conditions compared to the S–S and C–F support conditions. Additionally, it can be observed that in the C–F support condition, the first mode of free vibration generally exhibits a decrease followed by an increase as η approaches approximately 0.3. Moreover, these variations become more significant with an increase in the value of μ.

In another study, the effect of investigating the ratio of beam radius to beam height on its first natural frequency was examined. The network response for different values of the beam central angle was investigated. The material considered for this beam is homogeneous without reinforcing phase CNT, with concrete of characteristic strength 30 MPa and a beam radius of *5 m*. Fig. 17 illustrates this for different support conditions.

8. Conclusion

In summary, our investigation employed a hybrid approach, integrating FEM analysis with neural networks, to examine the behavior of carbon nanotube-reinforced curved beams. Our findings unveil a remarkable predictive precision exceeding 95 % concerning the initial

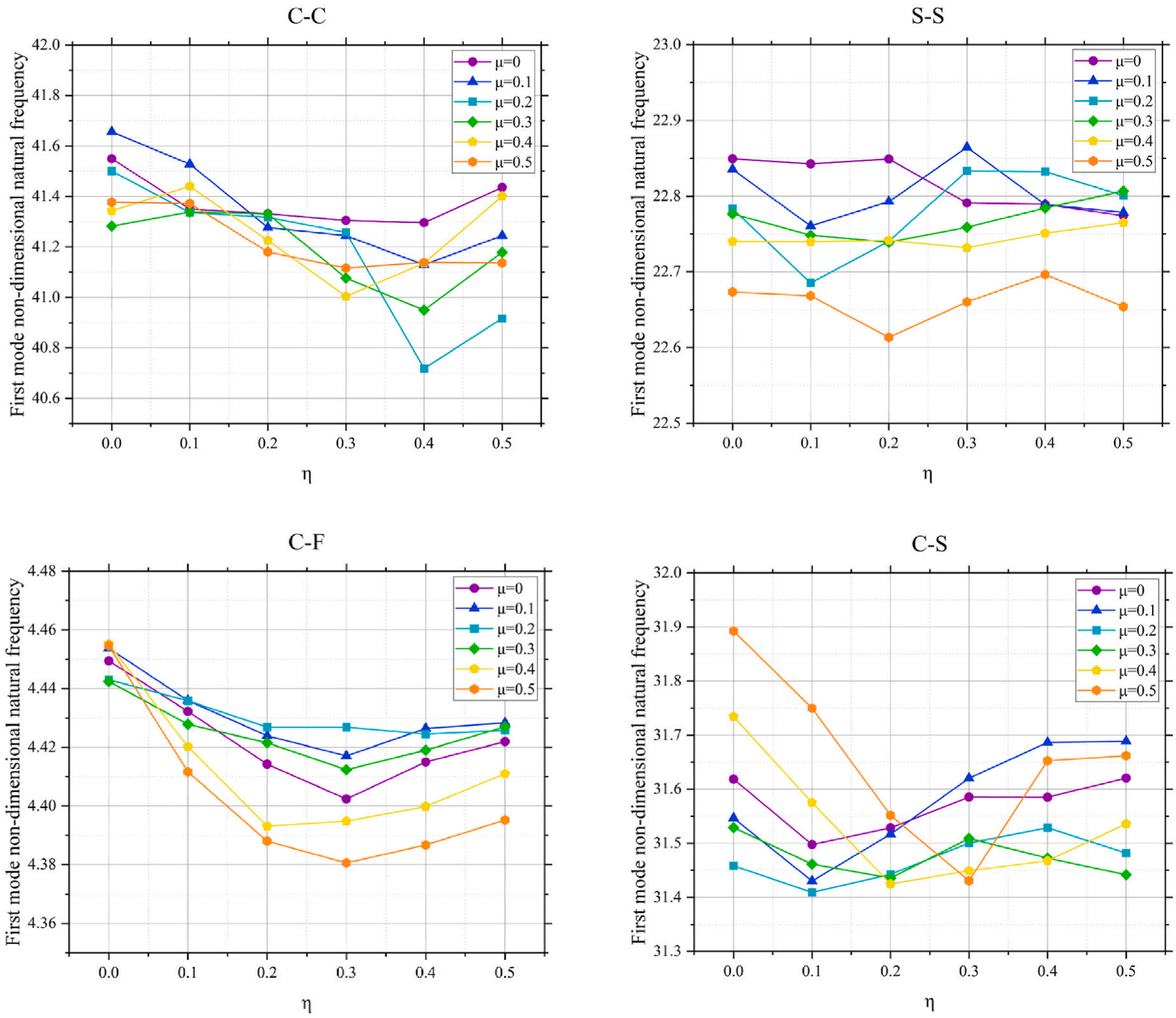

Fig. 16. Effect of η on the first dimensionless natural frequency for different support conditions.

natural frequency of the composite beams, underscoring the potential efficacy of neural network methodologies in engineering analyses. These outcomes not only enrich a comprehension of dynamic behaviors within composite structures but also furnish pragmatic insights for optimizing their efficacy in real-world scenarios. This inquiry establishes a robust groundwork for forthcoming endeavors aimed at augmenting the design and functionality of succeeding generations of composite materials, thereby reconciling conventional simulation methodologies with pioneering machine learning strategies. In summation, the results are as follows.

- Through our research endeavors, we attained a prediction accuracy exceeding 90 % concerning the initial natural frequency of carbon nanotube-reinforced curved beams employing our developed neural network architecture. Evidently, the model exhibited proficiency in accurately discerning the dynamic response of composite structures.
- Our neural network methodology showcased notable computational efficiency in contrast to conventional FEM analysis techniques. This delineates a pragmatic and time-saving avenue for scrutinizing intricate composite configurations.
- To ascertain the efficacy of our neural network model, we employed statistical metrics such as mean absolute error and root mean square error. These metrics corroborated our approach's dependability and resilience in forecasting the beams' vibrational attributes.
- Our meticulous analysis furnished invaluable insights into the dynamic behavior of carbon nanotube-reinforced curved beams under diverse mechanical and geometric circumstances. Such profound comprehension sets the stage for optimizing the design and functionality of composite structures across engineering domains.

Despite the numerous advancements and the high level of accuracy provided by the FEM in the analysis of curved beams, there exist several limitations that should be acknowledged. One of the prominent challenges lies in accurately modeling complex geometries and boundary conditions. This difficulty often results in numerical errors and inaccuracies in stress and displacement fields. Additionally, many FEM formulations heavily rely on assumptions and simplifications that may not adequately represent the nonlinear behaviors and anisotropy of materials. Another limitation of this study is that the application of the first-order shear deformation theory (Timoshenko beam theory) requires the use of shear correction factors, which is not simple for

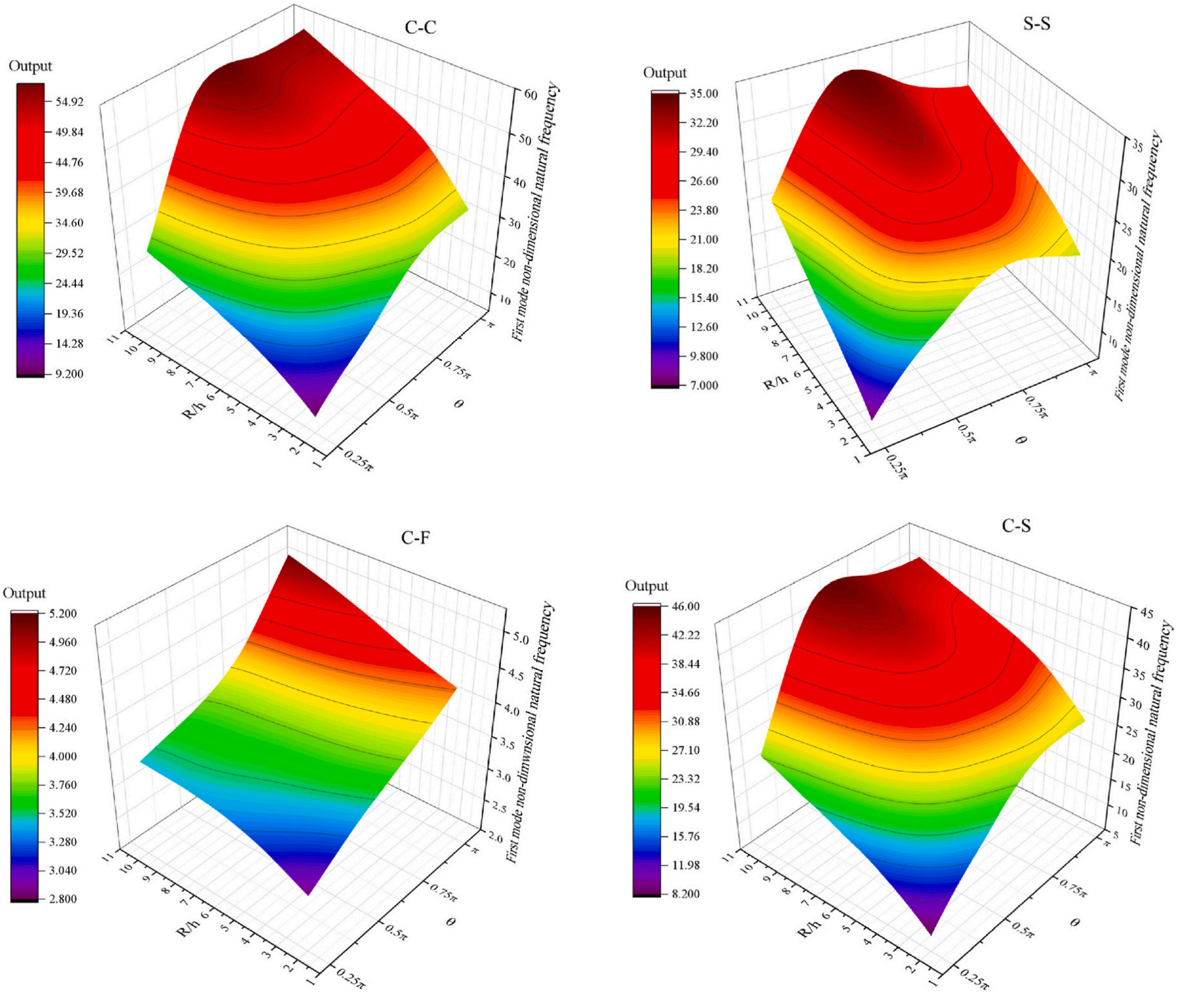

Fig. 17. Effect of θ and R/h on first dimensionless natural frequency for different support conditions.

composite materials. Furthermore, due to time and computational limitations, the data related to the neural network is limited, and only a subset of the beam's characteristics are considered as variables and introduced as input to the neural network. Conversely, certain variables, such as the radius and central angle of the beam, significantly impact the beam's amount of free vibration. Selecting these characteristics as input beyond their specified limits can lead to unacceptable errors. Consequently, there are some ideas for improvement in the future research. Some of these potential improvements are outlined below.

- Considering non-linear behavior for materials
- Utilizing the consistent mass matrix instead of the lumped mass matrix for beam dynamic analysis and comparing the results
- Considering the effect of higher-order shear deformations in the static and dynamic analyses of curved beams and comparing the results with Timoshenko beam theory.
- Investigating the sensitivity of the first mode of free vibration of the curved beam to each available mechanical and geometric characteristic
- Employing other neural network algorithms and comparing their accuracy and efficiency with the presented MLP model

CRediT authorship contribution statement

Hossein Mottaghi T: Writing – original draft, Validation, Software, Resources, Methodology, Investigation, Data curation. **Amir R. Masoodi:** Writing – review & editing, Writing – original draft, Visualization, Supervision, Methodology, Formal analysis, Conceptualization. **Amir H. Gandomi:** Writing – review & editing, Supervision, Resources.

Declaration of competing interest

The authors declare that they have no known competing financial interests or personal relationships that could have appeared to influence the work reported in this paper.

Data availability

Data will be made available on request.

Appendix A

Stiffness matrix of a curved element with 9 degrees of freedom in the local axis:

$$[K_l]=\begin{bmatrix}
\frac{7AE}{3R\theta}+\frac{2AGk\theta}{15R} & \frac{A(-E+Gk)}{2R} & \frac{2AGk\theta}{15} & -\frac{8AE}{3R\theta}+\frac{AGk\theta}{15R} & \frac{2A(-E-Gk)}{3R} & \frac{AGk\theta}{15} & \frac{AE}{3R\theta}-\frac{AGk\theta}{30R} & \frac{A(E+Gk)}{6R} & -\frac{AGk\theta}{30} \\
\frac{A(-E+Gk)}{2R} & \frac{2AE\theta}{15R}+\frac{7AGk}{3R\theta} & \frac{AGk}{2} & \frac{2A(E+Gk)}{3R} & \frac{AE\theta}{15R}-\frac{8AGk}{3R\theta} & \frac{2AGk}{3} & \frac{A(-E-Gk)}{6R} & -\frac{AE\theta}{30R}+\frac{AGk}{3R\theta} & -\frac{AGk}{6} \\
\frac{2AGk\theta}{15} & \frac{AGk}{2} & \frac{2AGR^2k\theta^2+35EI}{15R\theta} & \frac{AGk\theta}{15} & -\frac{2AGk}{3} & \frac{AGR^2k\theta^2-40EI}{15R\theta} & -\frac{AGk\theta}{30} & \frac{AGk}{6} & -\frac{AGRk\theta}{30}+\frac{EI}{3R\theta} \\
-\frac{8AE}{3R\theta}+\frac{AGk\theta}{15R} & \frac{2A(E+Gk)}{3R} & \frac{AGk\theta}{15} & \frac{16AE}{3R\theta}+\frac{8AGk\theta}{15R} & 0 & \frac{8AGk\theta}{15} & -\frac{8AE}{3R\theta}+\frac{AGk\theta}{15R} & \frac{2A(-E-Gk)}{3R} & \frac{AGk\theta}{15} \\
\frac{2A(-E-Gk)}{3R} & \frac{AE\theta}{15R}-\frac{8AGk}{3R\theta} & -\frac{2AGk}{3} & 0 & \frac{8AE\theta}{15R}+\frac{16AGk}{3R\theta} & 0 & \frac{2A(E+Gk)}{3R} & \frac{AE\theta}{15R}-\frac{8AGk}{3R\theta} & \frac{2AGk}{3} \\
\frac{AGk\theta}{15} & \frac{2AGk}{3} & \frac{AGR^2k\theta^2-40EI}{15R\theta} & \frac{8AGk\theta}{15} & 0 & \frac{8\left(AGR^2k\theta^2+10EI\right)}{15R\theta} & \frac{AGk\theta}{15} & -\frac{2AGk}{3} & \frac{AGR^2k\theta^2-40EI}{15R\theta} \\
\frac{AE}{3R\theta}-\frac{AGk\theta}{30R} & \frac{A(-E-Gk)}{6R} & -\frac{AGk\theta}{30} & -\frac{8AE}{3R\theta}+\frac{AGk\theta}{15R} & \frac{2A(E+Gk)}{3R} & \frac{AGk\theta}{15} & \frac{7AE}{3R\theta}+\frac{2AGk\theta}{15R} & \frac{A(E-Gk)}{2R} & \frac{2AGk\theta}{15} \\
\frac{A(E+Gk)}{6R} & -\frac{AE\theta}{30R}+\frac{AGk}{3R\theta} & \frac{AGk}{6} & \frac{2A(-E-Gk)}{3R} & \frac{AE\theta}{15R}-\frac{8AGk}{3R\theta} & -\frac{2AGk}{3} & \frac{A(E-Gk)}{2R} & \frac{2AE\theta}{15R}+\frac{7AGk}{3R\theta} & -\frac{AGk}{2} \\
-\frac{AGk\theta}{30} & -\frac{AGk}{6} & -\frac{AGRk\theta}{30}+\frac{EI}{3R\theta} & \frac{AGk\theta}{15} & \frac{2AGk}{3} & \frac{AGR^2k\theta^2-40EI}{15R\theta} & \frac{2AGk\theta}{15} & -\frac{AGk}{2} & \frac{2AGR^2k\theta^2+35EI}{15R\theta}
\end{bmatrix}$$

Effective stiffness matrix of curved elements with 6 degrees of freedom in the local axis:

$$K_{11}^{eff}=\frac{A\left(\begin{array}{c}-50AEG^2R^2k^2\theta^4\left(E\theta^2+10Gk\right)+2800E^2\left(E\theta^2+10Gk\right)\left(AGR^2k\theta^2+10EI+GIk\theta^2\right)+\\ 160EGk\theta^2\left(E\theta^2+10Gk\right)\left(AGR^2k\theta^2+10EI+GIk\theta^2\right)-1000E\theta^2(E+Gk)^2\left(AGR^2k\theta^2+10EI+GIk\theta^2\right)\\ -\left(40E-Gk\theta^2\right)\left(E\theta^2+10Gk\right)\left(AG^2R^2k^2\theta^4+\left(40E-Gk\theta^2\right)\left(AGR^2k\theta^2+10EI\right)\right)\end{array}\right)}{1200ER\theta\left(E\theta^2+10Gk\right)\left(AGR^2k\theta^2+10EI+GIk\theta^2\right)}$$

$$K_{12}^{eff}=\frac{A\left(\begin{array}{c}-50AEG^2R^2k^2\theta^2\left(E\theta^2+10Gk\right)-60E(E-Gk)\left(E\theta^2+10Gk\right)\left(AGR^2k\theta^2+10EI+GIk\theta^2\right)+10E(E+Gk)\left(E\theta^2-40Gk\right)\\ \left(AGR^2k\theta^2+10EI+GIk\theta^2\right)+(E+Gk)\left(E\theta^2+10Gk\right)\left(AG^2R^2k^2\theta^4+\left(40E-Gk\theta^2\right)\left(AGR^2k\theta^2+10EI\right)\right)\end{array}\right)}{120ER\left(E\theta^2+10Gk\right)\left(AGR^2k\theta^2+10EI+GIk\theta^2\right)}$$

$$K_{13}^{eff}=\frac{AGk\theta\left(3AEGR^2k\theta^4-20AEGR^2k\theta^2+10AG^2R^2k^2\theta^2+80E^2I\theta^2-200E^2I+3EGIk\theta^4-20EGIk\theta^2+600EGIk+10G^2Ik^2\theta^2\right)}{24\left(AEGR^2k\theta^4+10AG^2R^2k^2\theta^2+10E^2I\theta^2+EGIk\theta^4+100EGIk+10G^2Ik^2\theta^2\right)}$$

$$K_{14}^{eff}=\frac{A\left(\begin{array}{c}-50AEG^2R^2k^2\theta^4\left(E\theta^2+10Gk\right)+400E^2\left(E\theta^2+10Gk\right)\left(AGR^2k\theta^2+10EI+GIk\theta^2\right)-\\ 40EGk\theta^2\left(E\theta^2+10Gk\right)\left(AGR^2k\theta^2+10EI+GIk\theta^2\right)+1000E\theta^2(E+Gk)^2\left(AGR^2k\theta^2+10EI+GIk\theta^2\right)\\ -\left(40E-Gk\theta^2\right)\left(E\theta^2+10Gk\right)\left(AG^2R^2k^2\theta^4+\left(40E-Gk\theta^2\right)\left(AGR^2k\theta^2+10EI\right)\right)\end{array}\right)}{1200ER\theta\left(E\theta^2+10Gk\right)\left(AGR^2k\theta^2+10EI+GIk\theta^2\right)}$$

$$K_{15}^{eff}=\frac{A\left(\begin{array}{c}50AEG^2R^2k^2\theta^2\left(E\theta^2+10Gk\right)+10E(E+Gk)\left(E\theta^2-40Gk\right)\left(AGR^2k\theta^2+10EI+GIk\theta^2\right)+20E(E+Gk)\left(E\theta^2+10Gk\right)\\ \left(AGR^2k\theta^2+10EI+GIk\theta^2\right)-(E+Gk)\left(E\theta^2+10Gk\right)\left(AG^2R^2k^2\theta^4+\left(40E-Gk\theta^2\right)\left(AGR^2k\theta^2+10EI\right)\right)\end{array}\right)}{120ER\left(E\theta^2+10Gk\right)\left(AGR^2k\theta^2+10EI+GIk\theta^2\right)}$$

$$K_{16}^{eff}=\frac{AGk\theta\left(-AEGR^2k\theta^4+20AEGR^2k\theta^2+10AG^2R^2k^2\theta^2+40E^2I\theta^2+200E^2I-EGIk\theta^4+20EGIk\theta^2+600EGIk+10G^2Ik^2\theta^2\right)}{24\left(AEGR^2k\theta^4+10AG^2R^2k^2\theta^2+10E^2I\theta^2+EGIk\theta^4+100EGIk+10G^2Ik^2\theta^2\right)}$$

$$K_{22}^{eff}=\frac{A\left(\begin{array}{c}AE^2GR^2k\theta^6+64AEG^2R^2k^2\theta^4+40AG^3R^2k^3\theta^2+10E^3I\theta^4+3E^2GIk\theta^6-40E^2GIk\theta^4\\ +840E^2GIk\theta^2+84EG^2Ik^2\theta^4-400EG^2Ik^2\theta^2+2400EG^2Ik^2+40G^3Ik^3\theta^2\end{array}\right)}{24R\theta\left(AEGR^2k\theta^4+10AG^2R^2k^2\theta^2+10E^2I\theta^2+EGIk\theta^4+100EGIk+10G^2Ik^2\theta^2\right)}$$

$$K_{23}^{eff}=\frac{AGk\left(6AEGR^2k\theta^4+10AG^2R^2k^2\theta^2-5E^2I\theta^4+110E^2I\theta^2+6EGIk\theta^4-50EGIk\theta^2+600EGIk+10G^2Ik^2\theta^2\right)}{12\left(AEGR^2k\theta^4+10AG^2R^2k^2\theta^2+10E^2I\theta^2+EGIk\theta^4+100EGIk+10G^2Ik^2\theta^2\right)}$$

$$K_{24}^{eff}=\frac{A\left(\begin{array}{c}AG^2R^2k^2\theta^2\left(E\theta^2+10Gk\right)\left(-10E-Gk\theta^2+\theta^2(E+Gk)\right)-10E(E+Gk)\left(E\theta^2-40Gk\right)\left(AGR^2k\theta^2+10EI+GIk\theta^2\right)-20E\\(E+Gk)\left(E\theta^2+10Gk\right)\left(AGR^2k\theta^2+10EI+GIk\theta^2\right)-\left(40E-Gk\theta^2\right)\left(E\theta^2+10Gk\right)\left(AG^2R^2k^2\theta^2-(E+Gk)\left(AGR^2k\theta^2+10EI\right)\right)\end{array}\right)}{120ER\left(E\theta^2+10Gk\right)\left(AGR^2k\theta^2+10EI+GIk\theta^2\right)}$$

$$K_{25}^{eff}=\frac{A\left(\begin{array}{c}AE^2GR^2k\theta^6+56AEG^2R^2k^2\theta^4-40AG^3R^2k^3\theta^2+10E^3I\theta^4-E^2GIk\theta^6+40E^2GIk\theta^4\\+360E^2GIk\theta^2+36EG^2Ik^2\theta^4+400EG^2Ik^2\theta^2-2400EG^2Ik^2-40G^3Ik^3\theta^2\end{array}\right)}{24R\theta\left(AEGR^2k\theta^4+10AG^2R^2k^2\theta^2+10E^2I\theta^2+EGIk\theta^4+100EGIk+10G^2Ik^2\theta^2\right)}$$

$$K_{26}^{eff}=\frac{AGk\left(-4AEGR^2k\theta^4+10AG^2R^2k^2\theta^2-5E^2I\theta^4+10E^2I\theta^2-4EGIk\theta^4-50EGIk\theta^2+600EGIk+10G^2Ik^2\theta^2\right)}{12\left(AEGR^2k\theta^4+10AG^2R^2k^2\theta^2+10E^2I\theta^2+EGIk\theta^4+100EGIk+10G^2Ik^2\theta^2\right)}$$

$$K_{33}^{eff}=\frac{\left(\begin{array}{c}-50AEG^2IR^2k^2\theta^4\left(E\theta^2+10Gk\right)-1000AEG^2R^2k^2\theta^2\left(AGR^2k\theta^2+10EI+GIk\theta^2\right)+80E\left(E\theta^2+10Gk\right)\left(2AGR^2k\theta^2+35EI\right)\\\left(AGR^2k\theta^2+10EI+GIk\theta^2\right)+\left(E\theta^2+10Gk\right)\left(AGR^2k\theta^2-40EI\right)\left(AG^2R^2k^2\theta^4-\left(10E+Gk\theta^2\right)\left(AGR^2k\theta^2-40EI\right)\right)\end{array}\right)}{1200ER\theta\left(E\theta^2+10Gk\right)\left(AGR^2k\theta^2+10EI+GIk\theta^2\right)}$$

$$K_{34}^{eff}=\frac{AGk\theta\left(-AEGR^2k\theta^4+20AEGR^2k\theta^2+10AG^2R^2k^2\theta^2+40E^2I\theta^2+200E^2I-EGIk\theta^4+20EGIk\theta^2+600EGIk+10G^2Ik^2\theta^2\right)}{24\left(AEGR^2k\theta^4+10AG^2R^2k^2\theta^2+10E^2I\theta^2+EGIk\theta^4+100EGIk+10G^2Ik^2\theta^2\right)}$$

$$K_{35}^{eff}=\frac{AGk\left(4AEGR^2k\theta^4-10AG^2R^2k^2\theta^2+5E^2I\theta^4-10E^2I\theta^2+4EGIk\theta^4+50EGIk\theta^2-600EGIk-10G^2Ik^2\theta^2\right)}{12\left(AEGR^2k\theta^4+10AG^2R^2k^2\theta^2+10E^2I\theta^2+EGIk\theta^4+100EGIk+10G^2Ik^2\theta^2\right)}$$

$$K_{36}^{eff}=\frac{\left(\begin{array}{c}-A^2EG^2R^4k^2\theta^6+10A^2G^3R^4k^3\theta^4+16AE^2GIR^2k\theta^4-AEG^2IR^2k^2\theta^6+360AEG^2IR^2k^2\theta^2\\+10AG^3IR^2k^3\theta^4-240E^3I^2\theta^2-24E^2GI^2k\theta^4-2400E^2GI^2k-240EG^2I^2k^2\theta^2\end{array}\right)}{24R\theta\left(AEGR^2k\theta^4+10AG^2R^2k^2\theta^2+10E^2I\theta^2+EGIk\theta^4+100EGIk+10G^2Ik^2\theta^2\right)}$$

$$K_{44}^{eff}=\frac{A\left(\begin{array}{c}-50AEG^2R^2k^2\theta^4\left(E\theta^2+10Gk\right)+2800E^2\left(E\theta^2+10Gk\right)\left(AGR^2k\theta^2+10EI+GIk\theta^2\right)+\\160EGk\theta^2\left(E\theta^2+10Gk\right)\left(AGR^2k\theta^2+10EI+GIk\theta^2\right)-1000E\theta^2(E+Gk)^2\left(AGR^2k\theta^2+10EI+GIk\theta^2\right)\\-\left(40E-Gk\theta^2\right)\left(E\theta^2+10Gk\right)\left(AG^2R^2k^2\theta^4+\left(40E-Gk\theta^2\right)\left(AGR^2k\theta^2+10EI\right)\right)\end{array}\right)}{1200ER\theta\left(E\theta^2+10Gk\right)\left(AGR^2k\theta^2+10EI+GIk\theta^2\right)}$$

$$K_{45}^{eff}=\frac{A\left(\begin{array}{c}50AEG^2R^2k^2\theta^2\left(E\theta^2+10Gk\right)+60E(E-Gk)\left(E\theta^2+10Gk\right)\left(AGR^2k\theta^2+10EI+GIk\theta^2\right)-10E(E+Gk)\left(E\theta^2-40Gk\right)\\\left(AGR^2k\theta^2+10EI+GIk\theta^2\right)-(E+Gk)\left(E\theta^2+10Gk\right)\left(AG^2R^2k^2\theta^4+\left(40E-Gk\theta^2\right)\left(AGR^2k\theta^2+10EI\right)\right)\end{array}\right)}{120ER\left(E\theta^2+10Gk\right)\left(AGR^2k\theta^2+10EI+GIk\theta^2\right)}$$

$$K_{46}^{eff}=\frac{AGk\theta\left(3AEGR^2k\theta^4-20AEGR^2k\theta^2+10AG^2R^2k^2\theta^2+80E^2I\theta^2-200E^2I+3EGIk\theta^4-20EGIk\theta^2+600EGIk+10G^2Ik^2\theta^2\right)}{24\left(AEGR^2k\theta^4+10AG^2R^2k^2\theta^2+10E^2I\theta^2+EGIk\theta^4+100EGIk+10G^2Ik^2\theta^2\right)}$$

$$K_{55}^{eff}=\frac{A\left(\begin{array}{c}AE^2GR^2k\theta^6+64AEG^2R^2k^2\theta^4+40AG^3R^2k^3\theta^2+10E^3I\theta^4+3E^2GIk\theta^6-40E^2GIk\theta^4\\+840E^2GIk\theta^2+84EG^2Ik^2\theta^4-400EG^2Ik^2\theta^2+2400EG^2Ik^2+40G^3Ik^3\theta^2\end{array}\right)}{24R\theta\left(AEGR^2k\theta^4+10AG^2R^2k^2\theta^2+10E^2I\theta^2+EGIk\theta^4+100EGIk+10G^2Ik^2\theta^2\right)}$$

$$K_{56}^{eff}=\frac{AGk\left(-6AEGR^2k\theta^4-10AG^2R^2k^2\theta^2+5E^2I\theta^4-110E^2I\theta^2-6EGIk\theta^4+50EGIk\theta^2-600EGIk-10G^2Ik^2\theta^2\right)}{12\left(AEGR^2k\theta^4+10AG^2R^2k^2\theta^2+10E^2I\theta^2+EGIk\theta^4+100EGIk+10G^2Ik^2\theta^2\right)}$$

$$K_{66}^{eff}=\frac{\left(\begin{array}{c}-50AEG^2IR^2k^2\theta^4\left(E\theta^2+10Gk\right)-1000AEG^2R^2k^2\theta^2\left(AGR^2k\theta^2+10EI+GIk\theta^2\right)+80E\left(E\theta^2+10Gk\right)\left(2AGR^2k\theta^2+35EI\right)\\\left(AGR^2k\theta^2+10EI+GIk\theta^2\right)+\left(E\theta^2+10Gk\right)\left(AGR^2k\theta^2-40EI\right)\left(AG^2R^2k^2\theta^4-\left(10E+Gk\theta^2\right)\left(AGR^2k\theta^2-40EI\right)\right)\end{array}\right)}{1200ER\theta\left(E\theta^2+10Gk\right)\left(AGR^2k\theta^2+10EI+GIk\theta^2\right)}$$

References

[1] J.N. Reddy, An Introduction to the Finite Element Method, 1988, https://doi.org/10.1007/978-3-642-83535-3_3.

[2] C.S. Krishnamoorthy, Finite Element Analysis: Theory and Programming, Tata McGraw-Hill, 1994.

[3] O.C. Zienkiewicz, R.L. Taylor, J.Z. Zhu, The Finite Element Method Set, Elsevier, 2005, https://doi.org/10.1007/978-3-662-05358-4_2.

[4] K.-J. Bathe, H.A. Saunders, Finite element procedures in engineering analysis [Online]. Available:, 1982 https://api.semanticscholar.org/CorpusID:61522497.

[5] Mohammad Rezaiee-Pajand, Mohammad Moayedian, Mehran Kadkhodayan, Finite Element Theory, Islamic Azad University, Mashhad Branch 1 (2003).

[6] M. Rezaiee-Pajand, N. Rajabzadeh-Safaei, An explicit stiffness matrix for parabolic beam element, Lat. Am. J. Solid. Struct. 13 (9) (2016) 1782–1801, https://doi.org/10.1590/1679-78252820.

[7] S. Ghuku, K.N. Saha, A review on stress and deformation analysis of curved beams under large deflection, Int. J. Eng. Technol. 11 (2017), https://doi.org/10.18052/www.scipress.com/ijet.11.13.

[8] H. Upadhyay, N. Rao, P. Desai, Direct stiffness method for a curved beam and analysis of a curved beam using SAP, 2018 [Online]. Available: www.nuv.ac.

[9] J.K. Choi, A. Jang, K. Lim, SIMPLE CURVED SHEAR BEAM ELEMENTS, 1993.

[10] M.R. Banan, G. Karami, M. Farshad, FINITE ELEMENT ANALYSIS OF CURVED BEAMS ON ELASTIC FOUNDATIONS, 1989.

[11] P. Savino, F. Tondolo, Two-node curved inverse finite element formulations based on exact strain-displacement solution, Journal of Applied and Computational Mechanics 9 (1) (2023) 259–273, https://doi.org/10.22055/jacm.2022.41150.3708.

[12] J. Gon Kim, Y. Young Kims, A NEW HIGHER-ORDER HYBRID-MIXED CURVED BEAM ELEMENT, 1998.

[13] Z. Yang, X. Chen, Y. He, Z. He, J. Zhang, The analysis of curved beam using B-spline wavelet on interval finite element method, Shock Vib. 2014 (2014), https://doi.org/10.1155/2014/738162.

[14] J.Q. Tarn, W. Der Tseng, Exact analysis of curved beams and arches with arbitrary end conditions: a Hamiltonian state space approach, J. Elasticity 107 (1) (Mar. 2012) 39–63, https://doi.org/10.1007/s10659-011-9335-4.

[15] J.B. Kosmatka, Z. Friedman, Accurate two-node shear-deformable curved beam element, in: Collection of Technical Papers - AIAA/ASME/ASCE/AHS/ASC Structures, Structural Dynamics and Materials Conference, AIAA, 1998, pp. 157–167, https://doi.org/10.2514/6.1998-1716.

[16] E. Tufekci, U. Eroglu, S.A. Aya, A new two-noded curved beam finite element formulation based on exact solution, Eng. Comput. 33 (2) (Apr. 2017) 261–273, https://doi.org/10.1007/s00366-016-0470-1.

[17] A. H. Sheikh, "New Concept to Include Shear Deformation in a Curved Beam Element", doi: 10.1061/ASCE0733-94452002128:3406.

[18] Y. Wang, Improved strategy of two-node curved beam element based on the same beam's nodes information, Adv. Mater. Sci. Eng. 2021 (2021), https://doi.org/10.1155/2021/2093096.

[19] R.C. Hibbeler, Engineering Mechanics: Dynamics, eleventh ed., vol. 1, Pearson/Prentice Hall, 2007.

[20] A.k. Chopra, Dynamics of structures 5th edition SI units anul K chopra 5 (9) (2020).

[21] M. Williams, Structural Dynamics, 2016, https://doi.org/10.1201/9781315375311.

[22] F.Y. Cheng, Matrix Analysis of Structural Dynamics: Applications and Earthquake Engineering, 2017, https://doi.org/10.1201/9781315272467.

[23] M. Eisenberger, E. Efraim, In-plane vibrations of shear deformable curved beams, Int. J. Numer. Methods Eng. 52 (11) (Dec. 2001) 1221–1234, https://doi.org/10.1002/nme.246.

[24] M. Rezaiee-Pajand, N. Rajabzadeh-Safaei, Static and dynamic analysis of circular beams using explicit stiffness matrix, Struct. Eng. Mech. 60 (1) (Oct. 2016) 111–130, https://doi.org/10.12989/sem.2016.60.1.111.

[25] J.S. Wu, L.K. Chiang, Free vibration of a circularly curved Timoshenko beam normal to its initial plane using finite curved beam elements, Comput. Struct. 82 (29–30) (Nov. 2004) 2525–2540, https://doi.org/10.1016/j.compstruc.2004.05.020.

[26] J.S. Wu, L.K. Chiang, Free vibration analysis of arches using curved beam elements, Int. J. Numer. Methods Eng. 58 (13) (Dec. 2003) 1907–1936, https://doi.org/10.1002/nme.837.

[27] F. Yang, R. Sedaghati, E. Esmailzadeh, Free in-plane vibration of general curved beams using finite element method, J. Sound Vib. 318 (4–5) (Dec. 2008) 850–867, https://doi.org/10.1016/j.jsv.2008.04.041.

[28] J. Su, K. Zhou, Y. Qu, H. Hua, A variational formulation for vibration analysis of curved beams with arbitrary eccentric concentrated elements, Arch. Appl. Mech. 88 (7) (Jul. 2018) 1089–1104, https://doi.org/10.1007/s00419-018-1360-3.

[29] R.M. Corrêa, M. Arndt, R.D. Machado, Free in-plane vibration analysis of curved beams by the generalized/extended finite element method, Eur. J. Mech. Solid. 88 (Jul) (2021), https://doi.org/10.1016/j.euromechsol.2021.104244.

[30] W. J. Austin, F. Asce, A. S. Veletsos, and M. Asce, "JOURNAL OF THE ENGINEERING MECHANICS DIVISION FREE VmRATION OF ARCHES FLEXIDLE IN SHEAR 3.".

[31] Ö. Civalek, O. Kiracioglu, Free vibration analysis of timoshenko beams by DSC method, Int J Numer Method Biomed Eng 26 (12) (Dec. 2010) 1890–1898, https://doi.org/10.1002/cnm.1279.

[32] A. Karamanli, N. Wattanasakulpong, M. Lezgy-Nazargah, T.P. Vo, Bending, buckling and free vibration behaviours of 2D functionally graded curved beams, Structures 55 (Sep. 2023) 778–798, https://doi.org/10.1016/j.istruc.2023.06.052.

[33] M.O. Belarbi, A. Garg, M.S.A. Houari, H. Hirane, A. Tounsi, H.D. Chalak, A three-unknown refined shear beam element model for buckling analysis of functionally graded curved sandwich beams, Eng. Comput. 38 (Dec. 2022) 4273–4300, https://doi.org/10.1007/s00366-021-01452-1.

[34] M.O. Belarbi, M.S.A. Houari, H. Hirane, A.A. Daikh, S.P.A. Bordas, On the finite element analysis of functionally graded sandwich curved beams via a new refined higher order shear deformation theory, Compos. Struct. 279 (Jan) (2022), https://doi.org/10.1016/j.compstruct.2021.114715.

[35] M. Guerroudj, et al., Size-dependent free vibration analysis of multidirectional functionally graded nanobeams via a nonlocal strain gradient theory, J. Eng. Math. 146 (1) (Jun. 2024), https://doi.org/10.1007/s10665-024-10373-z.

[36] A. Frikha, S. Zghal, F. Dammak, Finite rotation three and four nodes shell elements for functionally graded carbon nanotubes-reinforced thin composite shells analysis, Comput. Methods Appl. Mech. Eng. 329 (Feb. 2018) 289–311, https://doi.org/10.1016/j.cma.2017.10.013.

[37] S. Zghal, A. Frikha, F. Dammak, Free vibration analysis of carbon nanotube-reinforced functionally graded composite shell structures, Appl. Math. Model. 53 (Jan. 2018) 132–155, https://doi.org/10.1016/j.apm.2017.08.021.

[38] S. Zghal, S. Trabelsi, F. Dammak, Post-buckling behavior of functionally graded and carbon-nanotubes based structures with different mechanical loadings, Mech. Base. Des. Struct. Mach. (2020) 1–43, https://doi.org/10.1080/15397734.2020.1790387.

[39] F. Kiarasi, A. Asadi, M. Babaei, K. Asemi, M. Hosseini, Dynamic analysis of functionally graded carbon nanotube (FGCNT) reinforced composite beam resting on viscoelastic foundation subjected to impulsive loading, J. Comput. Appl. Mech. 53 (1) (Mar. 2022) 1–22, https://doi.org/10.22059/jcamech.2022.339008.693.

[40] T. Zhao, M.J. Bayat, A. kalhori, K. Asemi, Free vibration analysis of functionally graded multilayer hybrid composite cylindrical shell panel reinforced by GPLs and CNTs surrounded by Winkler elastic foundation, Eng. Struct. 308 (Jun) (2024), https://doi.org/10.1016/j.engstruct.2024.117975.

[41] G. Hajdú, N. Bektaş, A. Müller, Machine learning models for the elastic-critical buckling moment of sinusoidal corrugated web beam, Results in Engineering 23 (Sep) (2024), https://doi.org/10.1016/j.rineng.2024.102371.

[42] M. Mohammed Sahib, G. Kovács, Multi-objective optimization of composite sandwich structures using artificial neural networks and genetic algorithm, Results in Engineering 21 (Mar) (2024), https://doi.org/10.1016/j.rineng.2024.101937.

[43] K. Aydin, O. Kisi, Damage detection in Timoshenko beam structures by multilayer perceptron and radial basis function networks, Neural Comput. Appl. 24 (3–4) (Mar. 2014) 583–597, https://doi.org/10.1007/s00521-012-1270-1.

[44] M. Turan, E. Uzun Yaylacı, M. Yaylacı, Free vibration and buckling of functionally graded porous beams using analytical, finite element, and artificial neural network methods, Arch. Appl. Mech. 93 (4) (Apr. 2023) 1351–1372, https://doi.org/10.1007/s00419-022-02332-w.

[45] F. Liu, X. Jiang, X. Wang, L. Wang, Machine learning-based design and optimization of curved beams for multistable structures and metamaterials, Extreme Mech Lett 41 (Nov) (2020), https://doi.org/10.1016/j.eml.2020.101002.

[46] A. Fallah, M.M. Aghdam, Physics-informed neural network for bending and free vibration analysis of three-dimensional functionally graded porous beam resting on elastic foundation, Eng. Comput. 40 (1) (Feb. 2024) 437–454, https://doi.org/10.1007/s00366-023-01799-7.

[47] N. Mohanty, S.K. Sasmal, U.K. Mishra, S.K. Sahu, Experimental and computational analysis of free in-plane vibration of curved beams, Journal of Vibration Engineering and Technologies 11 (4) (Jun. 2023) 1777–1796, https://doi.org/10.1007/s42417-022-00670-1.

[48] J. Yu, et al., Machine learning-based design and optimization of double curved beams for multi-stable honeycomb structures, Extreme Mech Lett 65 (Dec. 2023), https://doi.org/10.1016/j.eml.2023.102109.

[49] J. Zhang, X. Xue, Mechanical properties prediction and design of curved beams by neural network, Thin-Walled Struct. 195 (Feb) (2024), https://doi.org/10.1016/j.tws.2023.111434.

[50] T.T.H. Bui, T.T. Tran, D.K. Nguyen, Geometrically nonlinear analysis of sandwich composite beams reinforced by agglomeration carbon nanotubes, Vietnam J. Math. 44 (4) (Dec. 2022) 376–391, https://doi.org/10.15625/0866-7136/17911.

[51] E. Sobhani, A.R. Masoodi, A.R. Ahmadi-Pari, Vibration of FG-CNT and FG-GNP sandwich composite coupled Conical-Cylindrical-Conical shell, Compos. Struct. 273 (Oct) (2021), https://doi.org/10.1016/j.compstruct.2021.114281.

[52] J.N. Reddy, An Introduction to the Finite Element Method, 1988, https://doi.org/10.1007/978-3-642-83535-3_3.

[53] K.-J. Bathe, H.A. Saunders, Finite element procedures in engineering analysis, 1982 [Online]. Available: https://api.semanticscholar.org/CorpusID:61522497.

[54] Mohammad Rezaiee-Pajand, Theory of Matrix Structural Analysis, vol. 4, Ferdowsi university of Mashhad, 2015.

[55] L. Fausett, Fundamentals of Neural Networks: Architectures, Algorithms, and Applications, Prentice-Hall, Inc., USA, 1994.

[56] ACI Committee 318., American Concrete Institute., and International Organization for Standardization, Building Code Requirements for Structural Concrete (ACI 318-08) and Commentary, American Concrete Institute, 2008.

[57] Mohammad Rezaiee-Pajand, Mohammad Reza Salary, Structural Analysis 1, vol. 9, Imam Reza International University, 2013.